Northern and Southern Hemisphere Polar Cap Indices: to what extent do they agree and to what extent should they agree?

Michael Lockwood[1]

[1]University of Reading

June 16, 2023

Northern and Southern Hemisphere Polar Cap Indices: to what extent do they agree and to what extent should they agree?

M. Lockwood[1]

[1]Department of Meteorology, University of Reading, Reading, Berkshire, RG6 6BB, UK

Key Points:

- Simultaneous 1-minute values can differ, but the distributions of the north and south polar cap indices over 1998-2018 are very similar
- Both indices give significantly higher correlations with the predicted voltage of open flux generation and with observed transpolar voltage
- Both indices show a Russell-McPherron effect plus a northward-IMF lobe reconnection effect that is predominantly in the summer hemisphere

Corresponding author: Mike Lockwood, `m.lockwood@reading.ac.uk`

Abstract

The IAGA-endorsed Polar Cap Indices for the northern and southern hemispheres, *PCN* and *PCS*, are compared for 1998-2018, inclusive. Potential effects of the slightly-different, and changing, magnetic coordinates of the two magnetic stations employed, Thule (Qaanaaq) in Greenland and Vostok in Antarctica, are investigated. It is shown that the agreement in overall behaviour of the two indices is very close indeed but that *PCS* consistently correlates slightly better with solar wind parameters than *PCN*. Optimum lags for these correlations are 19 min for 1-min data and 37 min for hourly averages. The correlations are significantly highest for the predicted magnetopause reconnection voltage, which is a linear predictor of *PCN* and *PCS* for all 1-hour data and for all but the largest 0.1% of 1-min values. The indices show lower correlation and marked non-linearity (tending to saturation) at all levels with the estimated magnetopause reconnection electric field or the estimated power input into the magnetosphere. The *PCN* index is shown to correlate closely with the transpolar voltage measured by the northern-hemisphere SuperDARN radar network and both *PCN* and *PCS* clearly show the Russell-McPherron effect of dipole tilt and the Y-component of the interplanetary magnetic field. However the patterns in time-of-year and Universal Time (UT) are complicated by lobe reconnection during northward-IMF, the effect of which on the indices is shown to be predominantly a summer hemisphere phenomenon and gives a UT dependence on the IMF Y-component that is predicted theoretically.

Plain Language Summary

The Polar Cap Indices are generated from geomagnetic recordings made at Thule (Qaanaaq) in Greenland and Vostok in Antarctica and are used as monitors of the coupling of solar wind energy and momentum into Earth's magnetosphere. These stations are at similar locations relative to the nearby magnetic poles of the Earth but there are small differences, the effect of which is investigated. There has been debate about the processing of the data to generate the indices and the extent to which the results from the two hemisphere do - and should - agree with each other. It is shown that the overall agreement of the northern and southern hemisphere indices is very good indeed. It has been proposed that these indices reflect a number of aspects of coupling of the solar wind and Earth's magnetosphere, but it is shown here that they are optimum indicators of the voltage generated by magnetic reconnection between the geomagnetic field and the interplanetary magnetic field. This is shown to be consistent with the variations of the indices with time-of-year and time-of-day.

1 Introduction

1.1 The Polar Cap Index Stations

The Polar Cap Indices (PCI) are compiled using data from one magnetometer station in each hemisphere, each close to the geomagnetic pole (Stauning, 2021a, 2021b; Troshichev, 2022). The northern hemisphere index, *PCN*, is from observations made at the Thule (Qaanaaq) in Greenland (IAGA code THL: geographic coordinates 77.47°N, -69.23°E) and the southern hemisphere index, *PCS*, is from observations made at Vostok (IAGA code VOS: geographic coordinates -79.45°N, 106.87°E). (IAGA is the International Association of Geomagnetism and Aeronomy, one of the eight associations of the International Union of Geodesy and Geophysics). Over the years studied in this paper (1998-2018) there has been a relatively rapid motion of the Northern geomagnetic (eccentric dipole) pole towards the rotational axis and much slower motion of the Southern pole (Koochak & Fraser-Smith, 2017; Lockwood et al., 2021). This has resulted in different motions of the stations in geomagnetic coordinates. This paper employs the Altitude-Adjusted Corrected Geomagnetic Coordinate system AACGMv2 (Shepherd, 2014) and the magnetic coordinates of the two stations in this frame are given in Table 1 for the

Table 1. AACGMv2 magnetic coordinates of the PCI stations Thule (THL) and Vostok (VOS)

Year	Lat. $^\circ N$	Lat. $^\circ N$	Long $^\circ E$	Long $^\circ E$
	THL	VOS	THL	VOS
1998	85.17	-83.34	32.28	54.86
2010	84.40	-83.58	28.31	55.48
2021	83.67	-83.80	24.24	55.93

start, middle and end years of the period studied. This shows 1.50° equatorward motion of THL in the geomagnetic frame over the interval, while VOS moved 0.46° poleward. Over the same interval, THL moved 8.04° westward in this frame whereas VOS moved 1.07° eastward.

AACGMv2 coordinates at the Earth's surface are essentially a map of the higher-order International Geophysical Reference Field (IGRF) model to a simple tilted, centred dipole model. This mapping is performed by tracing an IGRF field line (using the IGRF model appropriate to the date in question) to the dipole magnetic equatorial plane and then tracing the dipole field line from that point back to the surface. A way to further understand the locations of the PCI stations, relative to the magnetic poles, is to compare the geographic coordinates of the station with those of the nearby magnetic pole: to do this, we need to be clear about which type of magnetic pole we are comparing with.

Parts (a) and (d) of Figure 1 are maps showing the locations of the PCI magnetometer stations, THL and VOS. Also shown are the locations of the magnetic poles for 1980, 2000 and 2020. The blue dots are the pole locations for a geocentric dipole model, obtained by taking the first three terms of the spherical harmonic expansion (the "Gauss coefficients") of the IGRF model. The mauve dots are for a more realistic eccentric dipole model, obtained by using the first 8 IGRF Gauss coefficients. It can be seen in part (d) that VOS lies very close to the south geocentric pole, particularly around the year 2000. However, part (a) shows that THL lies equatorward of the geocentric poles and that difference has grown since 1980. This difference is even greater for the more realistic eccentric field model for which VOS is approximately 5° poleward of the magnetic pole, whereas THL was 9° equatorward of the magnetic pole in 1980, rising to 15° in 2020. Hence there are considerable differences between the north and south PCI station locations, relative to their local magnetic pole.

These shifts have an effect on the variations in magnetic local time (MLT) of the stations over the day. Figure 1 shows the variations of the difference between Magnetic Local Time (MLT) and Universal Time (UT) as a function of UT for the PCI stations. These are calculated using equation 1 and the AACGMv2 coordinate system in which Thule/Qaanaaq (THL, which gives PCN) is at a magnetic latitude of 85.17°N at the start of the interval studied (1998) and 83.67°N at its end (2021, if provisional data are included), as shown in Table 1. This table also shows a much smaller change in the magnetic latitude of Vostok (VOS, which gives PCS) in the same interval, from -83.34°N to -83.80°. MLT is a parameter that needs defining as it depends on both the coordinate system and the definition adopted. For model field lines that do not cross the Earth's magnetic equatorial plane, definitions of MLT based on the position of that crossing point cannot be used. This paper uses the definition given by Laundal and Richmond (2017):

$$MLT_p = 12 + (\phi_{P,X} - \phi_{S,CD})/15 \quad (1)$$

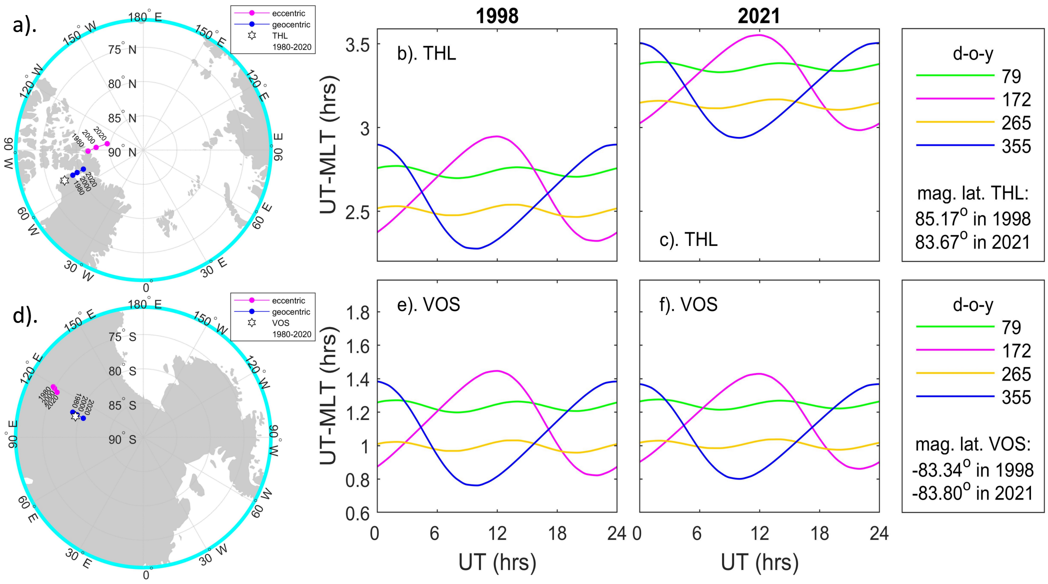

Figure 1. Part (a) and (d) show the locations of the PCI stations, for the northern and southern polar cap, respectively, relative to the corresponding magnetic and rotational poles. The blue points are for a geocentric dipole model of Earth's field and the mauve dots for an eccentric dipole model. Locations for 1980, 2000 and 2020 are shown. The magnetometer location is shown by the white star and the rotation poles at $+90°$ and $-90°$ for the North and South, respectively. Parts (b), (c), (e) and (f) show the Variations of the difference between Magnetic Local Time (MLT) and Universal Time (UT) for the two Polar Cap Index stations, as a function of UT. Parts (b) and (c) are for THL, (d) and (e) for VOS. The middle column, (parts b and d), is for 1998; the right-hand, (parts e and f), for 2021. Curves are for: (green) March equinox (day-of-year 79, fraction of year $F = 0.22$); (mauve) June solstice (d-o-y 172, $F = 0.47$); (orange) September equinox (d-o-y 265, $F = 0.73$); and (blue) December solstice (d-o-y 355, $F = 0.97$).

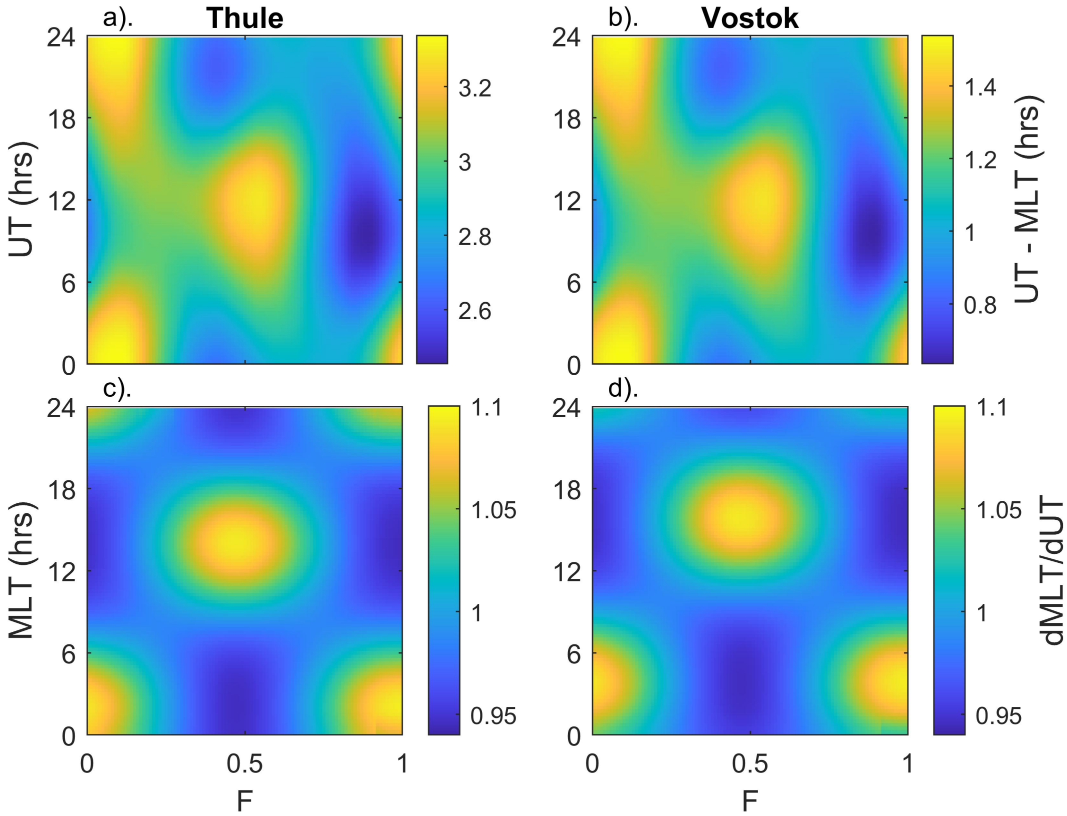

Figure 2. (Top) Fraction of year F - Universal Time UT plots of UT-MLT for 2010 (the middle of the period of interest) (Bottom) The corresponding gradient of MLT with UT shown as a function of F and MLT. (a) and (c) are for Thule, (b) and (d) for Vostok. MLT is computed as in Figure 1.

where MLT_p is the MLT of the point P in hours and $\phi_{P,X}$ is its magnetic longitude in coordinate system "X". $\phi_{S,CD}$ is the magnetic longitude of the subsolar point in centered dipole ("CD") coordinates. The use of CD coordinates at S provides a standard reference point but $\phi_{P,X}$, and hence MLT_p depends on the coordinate system X adopted. Figure 1 uses the AACGMv2 coordinate system, but calculations were repeated using the original AACGM coordinates (Baker & Wing, 1989) (the procedure also used by the SuperMAG project). The variations with UT and time of year are very similar in all cases but the changes between 1998 and 2021 were smaller for AACGM coordinates.

Figure 1 shows a characteristic variation of *(UT-MLT)* with both UT and time-of-year F that is caused by the factor $\phi_{S,CD}$. The large shift in the magnetic coordinates of THL over the years studied causes a large shift in the pattern to larger *(UT-MLT)* whereas the corresponding shift for VOS is small.

The top row of Figure 2 looks at the pattern in faction of year (F) and Universal Time (UT) of *(UT-MLT)* for 2010 (the middle of the period studied in the paper). The plots are very similar in form except for the scales, with values being about 1.8 hrs higher for Thule than for Vostok. The bottom panels reveal an interesting implication of this, showing the variation of the ratio $dMLT/dUT$ as a function of F and MLT. The variations are very similar but the shift in the scale in (b) relative to (a) causes the pattern to be at slightly higher MLT in (d) than in (c). These patterns may have an interesting effect on the data. To illustrate this point, let us look at $13h$ MLT in mid-summer

($F = 0.5$ for Thule and $F = 0$ or 1 for Vostok). This location is of interest as it is where one expects most often to see the effects of lobe reconnection when the IMF points northward (Crooker & Rich, 1993). Figure 2c shows that for Thule $dMLT/dUT \approx 1.1$ at this location whereas 2d shows that for Vostok it is ≈ 0.95. This means that Thule spends 10% less time than the average at this location whereas Vostok spends 5% more time than the average there. The net result is that Vostok spends 16% more time in the region where lobe reconnection signatures are expected to be most common from this effect. This effect is in addition to any consequences of the magnetic latitude difference of the stations which was near 1.8° in 1998 but reduced to near zero by 2021.

It should be noted that the scaling of the PCN and PCS data depends on the geometry of the geomagnetic field and so should ideally be adjusted with time to allow for these changes in Earth's intrinsic field, but such a correction has not yet been implemented in any of the iterations of the PCI indices. The PCI have a complicated history of corrections and improvements that is only briefly outlined in Sections 1.2 and 2. This means that care must be taken when comparing conclusions of the present study to those of past studies as different versions of the indices may have been used.

1.2 Generation of The Polar Cap Indices

The PCN and PCS indices are derived from enhancements of the horizontal H and D magnetic field components relative to the quiet level at two the polar cap stations, Thule and Vostok. The dipole tilt has a major effect on the ionospheric conductivity which, in turn, has a major effect on the magnetic deflection seen at the PCI stations. In particular, the equivalent winter DP2 currents are deflected counter clockwise through angles 20-60° relative to the summer DP2 currents (Maezawa, 1976). These conductivity effects are allowed for (at least partially) by taking the difference with respect to a quiet-day reference ΔF which is related to the solar wind forcing of the polar currents and flows and was found by Troshichev and Andrezen (1985) to correlate highly with the magnetopause reconnection rate (the electric field along the reconnection line, E_m), predicted from an empirical coupling function and observed solar wind parameters. The coupling function used is that by Kan and Lee (1979), which is

$$E_m = V_{sw} B_t sin^2(\theta/2) \tag{2}$$

where V_{sw} is the solar wind speed in the -X direction, $B_t = (B_X^2 + B_Y^2)^{1/2}$ is the transverse component of the IMF and $\theta = atan(|B_Y|/B_Z)$ is the clock angle of the IMF, all IMF components and θ being measured in the GSM frame of reference. Note that this is an early version of a great many such coupling functions that have been proposed, as recently reviewed by Lockwood and McWilliams (2021a).

Using three parameters α, β and ϕ for the station in question, a statistical relationship between ΔF and E_m that works at all UT has been developed and shown to remain valid throughout solar cycles 23 and 24 by Troshichev et al. (2022b). Note that although this relationship varies with UT and time-of-year, it has not been varied from year to year to allow for changes in the geomagnetic field discussed in Section 1.1.

However, a caveat should be noted about ΔF as it is assumed that the conductivity effect on the quiet day and the observed day are the same and so ΔF depends only on the solar wind forcing. This may not always be the case, for example if there is strong local electron precipitation or a strong flux of EUV/X-ray photons from a solar flare on the observed day. These effects need not influence both hemispheres in the same way and so although the method will remove the effect of regular dipole-tilt-induced variations in conductivity there may be incidents of discrepancy introduced asymmetrically into PCN and PCS by unusual conductivity-enhancing events in one polar cap.

The statistical relationship used converts the observed ΔF value into an E_m estimate and so the PCI indices are given in units of mVm^{-1}. However, (Lockwood & Milan, 2023) point out that the ΔF value is a magnetic field measurement and so does not depend on the frame of measurement. The same is true of the PCI indices because there is nothing in the regression that converts ΔF into a PCI value that accounts for the fact that the observing stations are moving in a geocentric-solar frame (such as GSE, GSM or GSEQ); this motion being due to Earth's rotation and the offset of the station geographic latitude from the rotational pole. Unlike magnetic fields, electric fields do depend on the frame of reference and so genuine electric field measurement would need transformation into a geocentric-solar frame, but because they are based on a magnetic field measurement (ΔF), the PCI values do not need such a transformation even though they are given in units of electric field (mVm^{-1}).

The PC indices have been issued from the Arctic and Antarctic Research Institute (AARI) in St. Petersburg, the Danish Meteorological Institute (DMI), and the Danish Space Research Institute (DTU Space) in different versions over the years since the pioneering work of Troshichev et al. (1988). The present paper examines the *PCN* and *PCS* data sets that were initially recommended by IAGA in 2013 (Menvielle et al., 2013) and recently endorsed for full scientific use in (IAGA Resolution #2, 2021; see `https://www.iaga-aiga.org/resolutions/resolution-no-2-2021-polar-cap-pc-index/`). These data are retrieved from the International Service of Geomagnetic Indices (ISGI) from `https://isgi.unistra.fr/geomagnetic_indices.php`.

The *PCN* data were compiled by DTU Space based on prior issues of definitive values. Both indices have been through a series of corrections and improvements. The *PCN* index series developed at DMI (Vennerstrøm, 2019) contained some errors that were uncorrected when transferred to DTU Space in 2009. The *PCS* data were based on a refurbished set of preliminary values issued between 2013 and 2021. These preliminary *PCS* data contained some errors that were not corrected in some early publications (Stauning, 2022b, 2022a). Before 2013, IAGA endorsement of the indices was not forthcoming because of concerns that the procedure used was not the same for the two indices (McCreadie & Menvielle, 2010; Stauning, 2013). Although the two were highly correlated, *PCN* was systematically 35% smaller than *PCS* and the difference grew when values were high (Lukianova et al., 2002; Ridley & Kihn, 2004). This first raised the question how much the differences between *PCN* and *PCS* were due to processing differences, or station location or instrumentation differences, or physical hemispheric differences between the two polar caps.

Subsequently, a "unified method" of processing was developed at AARI (Troshichev et al., 2006) but subsequent calibration errors were discovered and after the 2013 IAGA Resolution both the *PCN* and *PCS* indices were re-calculated at DTU Space and at AARI using a corrected and improved version of the unified method (Matzka & Troshichev, 2014). Note the changes to processing have involved changes to the quiet-day background quantification. Hence the reader needs to bear in mind that past publications were often using different versions of *PCN* and *PCS* data series to that employed in the present paper and so comparisons with past papers would not be fully valid.

All the IAGA-endorsed definitive data have been re-generated using the corrected unified method, a task that was completed in 2021 and several anomalies resolved. The full details of the development of the indices to this point are beyond the scope of the present paper. However, the revision rekindled the debate in the literature about the level of agreement between *PCN* and *PCS*. This debate divided into two parts. The first dealt with the generality of the procedures applied to *PCS* (Lukianova, 2007; Troshichev et al., 2007), the point being that if the corrections are too tailored to solving existing anomalies, they may well not apply to future data. The second related to times about outstanding differences between the two indices (Stauning, 2022a, 2022b; Troshichev et al., 2022a). It is certainly true that considerably greater agreement between *PCS* and *PCN* exists in the IAGA-approved version of the data than used to be the case before application of the unified method, to the extent that remaining differences between PCS and PCN may well be real and it could be the expectation that they should be the same that may be in error.

1.3 Induction effects and electric field mapping

Differences between PCN and PCS raise a host of issues that depend on what the PCI are viewed as being a metric of. The generation of the PCI requires ΔF be scaled as E_m, a coupling function derived from interplanetary measurements. Hence PCI can be thought of as a metric of electric field in interplanetary space, E_{sw}, the electric field along the magnetopause reconnection X-line, E_m or the electric field in the polar ionosphere, E_i. In addition, from comparisons with convection patterns derived from a variety of observations using the AMIE (Assimilative Mapping of Ionospheric Electrodynamics) technique, Ridley and Kihn (2004) found the PCI correlated best with transpolar voltage (i.e., the cross-cap potential drop, Φ_{PC}), a relationship also reported by Troshichev et al. (1988). Other studies have used PCI as metrics of ionospheric Joule heating (Chun et al., 1999) and/or energy input into the magnetosphere (Troshichev, 2022).

If the electric fields, E_{sw}, E_m and E_i are viewed as being the same, then PCN should always be identical to PCS as both would be set by the interplanetary electric field. However, E_{sw}, E_m and E_i are are not, in general, the same. The reason they can differ is non-steady conditions. This is the third of the three key founding principles of the Expanding-Contracting Polar Cap (ECPC) model of ionospheric convection excitation (Cowley & Lockwood, 1992) that has explained observed features on ionospheric convection (see reviews by Lockwood & Cowley, 2022; Lockwood & McWilliams, 2021b, and references therein). The three are the continuity of open flux (Holzer et al., 1986), the effect of moving "adiaroic" (non-reconnecting) polar cap boundaries (Siscoe & Huang, 1985), and the inductive decoupling of solar wind and magnetospheric electric field in non-steady conditions (Lockwood & Cowley, 1992; Lockwood & Milan, 2023; Lockwood & Morley, 2004; Lockwood et al., 1990).

In general, there are changes in the magnetospheric and magnetosheath magnetic fields and, by Faraday's law, this means there is a curl to the electric field and inductive decoupling of the electric field along field lines. As a result, at any one time E_{sw}, E_m and E_i, will, in general, all be different and so the ionospheric electric field in the southern hemisphere ionospheric polar cap, E_{Si}, can be different from that in the northern E_{Ni}. Hence PCS can differ from PCN at any one time. Only in steady state (where $dB/dt = 0$ everywhere) should we expect PCN and PCS to be identically the same. Because long-term trends in the magnetosphere are negligibly small, conditions approach steady state as the averaging timescale, τ, is increased. Hence although PCN and PCS can differ for $\tau = 1$min, the expectation is that, if they are properly calibrated, they will converge as τ is increased. This paper mainly considers two values of τ: (1) the 1-minute integration timescale of the raw data and (2) $\tau = 1$hr, which averages over a typical substorm cycle and allows comparison with the SuperDARN transpolar voltage data (Lockwood & McWilliams, 2021b). In addition, some summary analysis was carried out for $\tau = 1$ day, which averages over several substorm cycles and all but the largest magnetic storms, $\tau = 1$ yr, and all data (24 years).

Decoupling of the solar wind, reconnection and transpolar voltages is often, incorrectly, thought of as showing non-ideal-MHD electrostatic field-aligned potential drops (e.g. Merkine et al., 2003). This is incorrect because time-dependent situations are explicitly not static: ideal MHD is based on Maxwell's equations, including Faraday's law that states that the electric field integrated around a loop is equal to the rate of change in the magnetic flux treading the loop. MHD models of the magnetosphere clearly demonstrate that electric field and voltages do not map from the solar wind to the ionosphere. In the example simulations by Connor et al. (2014), the time variations are introduced by solar wind dynamic pressures pulses which raise the magnetic shear across current sheets and so enhance the magnetic reconnection rates. This happens first in the dayside magnetopause (raising the magnetopause reconnection voltage Φ_D) and later in the cross-tail current sheet (raising the tail reconnection rate Φ_N) and the transpolar voltage (Φ_{PC}) is different from both most of the time. The effect is most extreme in their Figure 5 in which the simultaneous one-minute modelled values at 23:40 UT (after the pressure pulse) were Φ_{PC} = 120 kV, Φ_D = 193 kV and Φ_N =53 kV; at 23:10 they were Φ_{PC} = 107 kV, Φ_D = 65 kV and Φ_N = 185 kV; and at 22:48 were Φ_{PC} = 91 kV, Φ_N = 35 kV and Φ_D = 35 kV. Hence the induction effects are causing the voltages to differ by factors of up to 3 whereas for steady state they would all be the same. The same effects are seen in the simulations presented by Lockwood, Owens, Barnard, Watt, et al. (2020). This means we should expect times when PCN and PCS differ by factors this large on short timescales but differences will shrink as averaging timescale τ are increased, as the values become increasingly representative of steady state conditions. Note that responses to pressure pulses in the Polar Cap Indices have been observed by Lukianova (2003) and by Stauning and Troshichev (2008). Similar divergences of Φ_{PC}, Φ_N and Φ_D was simulated by Gordeev et al. (2011) who used an MHD model to simulate time-dependent cases caused by IMF orientation changes.

Induction effects are often discussed in different ways. For example, Borovsky and Birn (2014) discuss the variability of the magnetopause reconnection rate (the electric field along the reconnection X-line) as being not controlled by the electric field in interplanetary space. If the magnetosheath field between the two were constant, this would not be the case and the reconnection rate would be the interplanetary electric field times a mapping factor that would be constant. Hence what Borovsky and Birn (2014) are pointing out is that the induction effects are so important and great that the reconnection rate is effectively decoupled from the interplanetary electric field on all but the longest timescales.

1.4 Conductivity effects

The annual and daily variations in the tilt of the dipole field with respect to the Sun-Earth line changes the solar zenith angles at locations inside the polar caps and auroral oval and hence modulates the EUV-generated ionospheric conductivities (Brekke & Moen, 1993). This effect has been invoked many times in the context of UT variations in geomagnetic activity (for example Lyatsky et al., 2001; Newell et al., 2002; Ridley et al., 2004; Wang & Lühr, 2007). An important consideration is that enhanced solar EUV radiation (through lower solar zenith angles) is often only the secondary source of enhanced conductivity after particle precipitation, particularly in the auroral ovals (Kubota et al., 2017). The precipitation source is highly variable in space and time (Carter et al., 2020; B. Zhang et al., 2015).

As discussed above, the method of derivation of the PCI indices largely gives removal of conductivity effects induced by the regular dipole tilt variations. However, there are reasons to expect transpolar voltages and electric fields to vary with ionospheric conductivity and so these effects would increase the scatter in relationships between the PCI and transpolar voltage Φ_{PC}.

The effect of enhanced conductivity in a polar cap is that F-region ionospheric flow speed, ionospheric electric field and transpolar voltage are all reduced (Ridley et al., 2004): if caused by the dipole tilt effect on conductivity, these would all be simultaneously enhanced in the other polar cap by the lower conductivity. The upstream solar wind, of course, has no information about either change and so this causes scatter in the scaling of PCN and PCS in terms of the solar wind coupling function but does not influence the average fit. This conductivity effect is widely invoked as the cause of “saturation”, in which enhanced conductivity gives rise to lower-than-expected transpolar voltages when solar wind-magnetosphere coupling is exceptionally strong and even makes them tend asymptotically to an upper limit (Hairston et al., 2003; Orr et al., 2022; Russell et al., 2001; Shepherd, 2007). However, it is worth noting the caveat on the concept of saturation that the deviation from the expectation may mean that the expectation is incorrect for large values of solar wind forcing (Sivadas et al., 2022): the regression of the transpolar voltage and a solar wind forcing coupling function will, for simple regression procedures, have been statistically weighted towards the mean values and may well be incorrect at larger values (Lockwood, 2022; Sivadas & Sibeck, 2022).

When considering the potential effect of ionospheric conductivity and flux transport, it is vital to consider Maxwell's equation $\nabla \cdot \vec{B} = 0$ (the non-existence of magnetic monopoles). Because open flux is only generated and lost by magnetic reconnections which change the open flux in both hemispheres by the same amount, this demands that the open flux in the two hemispheres must be identical at any instant. Lobe reconnection during northward IMF (discussed in section 1.5) in one hemisphere changes the configuration of open flux but not the total amount and lobe reconnection in both hemispheres reduces the open flux in the two hemispheres equally. In addition, when integrated/averaged over sufficient time, the antisunward magnetic flux transport rate of open flux in both ionospheric polar caps (i.e, the transpolar voltages) must be the same as that of the parts of the open field lines that are in interplanetary space or $\nabla \cdot \vec{B} = 0$ is violated. This consideration leads to many of the proposed mechanisms for explaining saturation effects invoking a mechanism that imposes a limitation to the reconnection voltage at the dayside magnetopause (Siscoe, 2002). However, this means that the time-averaged voltage would be reduced equally in both polar caps by enhancements to the conductivity in either polar cap.

An alternative explanation of saturation effects is provided by inductive effects which reduce the flow in only the polar cap in which the conductivity is enhanced. However, such a mechanism can only smooth out peaks and troughs in the reconnection voltage such that the enhancement/decrease in transpolar voltage is smaller but lasts longer. Several numerical simulations confirm that increased polar cap conductivity reduces transpolar voltages on shorter timescales (Borovsky et al., 2009; Kubota et al., 2017; Merkine et al., 2003; Raeder et al., 2001). This is to be expected because field-perpendicular conductivity (both Hall and Pedersen) arise from collisions between ions and electrons and neutral atoms and these collisions also give frictional drag on the motion of F-region plasma and frozen-in magnetic field (Ridley et al., 2004). As discussed by Tanaka (2007) and (for an isolated flux tube) by Southwood (1987), this is the "line-tying" concept introduced by Atkinson (1967) and Atkinson (1978) to explain the origin of field-aligned currents and how they transfer momentum and energy down into the ionosphere. Lockwood and Milan (2023), describe how the slowing of the flow in the ionosphere, but not in the solar wind, means that the lobe flux in that hemisphere grows faster, thereby shifting the locations of the magnetopause and the cross-tail current sheet. This is seen in model results; for example, in the MHD simulation of the Bastille day storm by Raeder et al. (2001), the lobes swell so much that the magnetospheric shape becomes distorted. This means that enhanced conductivity is really influencing the balance between energy stored in the tail (and later released) and energy directly deposited in the ionosphere. This explanation of conductivity effects can therefore influence the transpolar voltage in one polar cap but not the other; but note that, unless one is invoking magnetic monopoles (which have never been definitively detected), this effect must average out on long timescales. Hence induction effects mean that simultaneous PCN and PCS can differ considerably (from the MHD simulations discussed above by a factor of at least 3) but should agree in averages and distributions taken over long timescales.

Given the way that the PCI are constructed, we should not expect to see a saturation effect in them as they are scaled to upstream solar wind parameters. However,

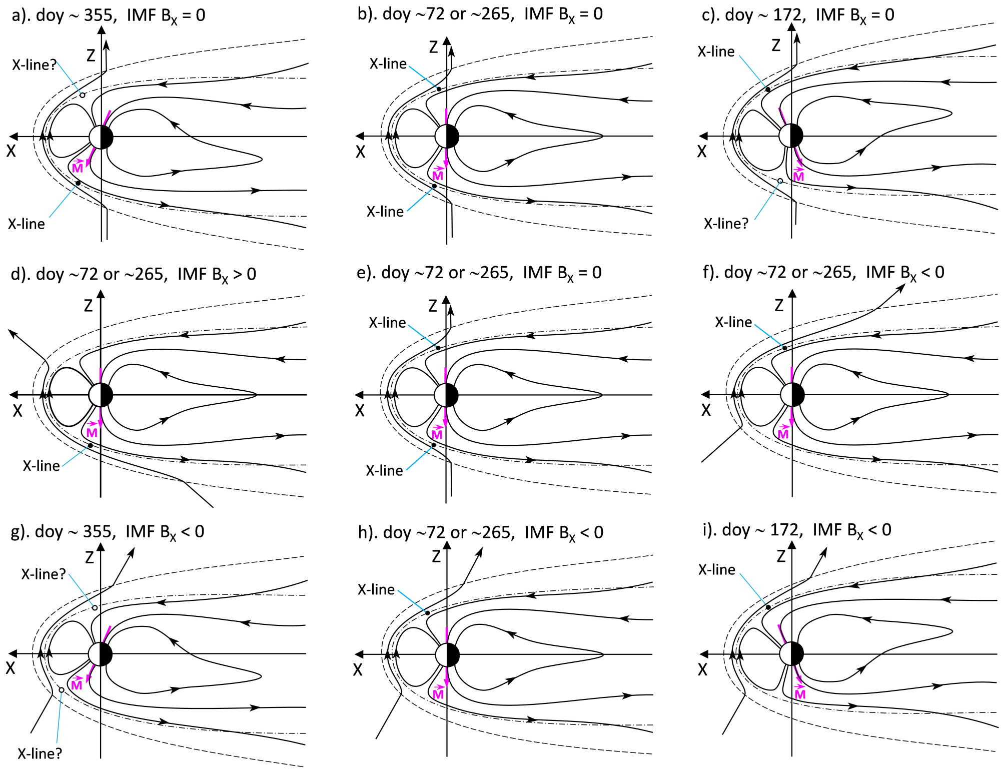

Figure 3. Schematic illustrations of the most likely lobe reconnection sites (marked"X-line") during northward IMF ($B_Z > 0$). The top row is for $B_X = 0$ and around (a) the December solstice, (b) the equinoxes and (c) the June solstice. The middle row are for around the equinoxes and are for IMF (d) $B_X > 0$, (e) $B_X = 0$ (and so part e is the same as part b) and (f) ($B_X < 0$. The bottom row are for IMF $B_X < 0$ and around (g) the December solstice, (h) the equinoxes and (i) the June solstice. Probable reconnection sites are marked with black filled circles, possible but unlikely ones with open circles. (after Lockwood & Moen, 1999).

Nagatsuma (2004) found that *PCN* does show saturation when the estimated dayside reconnection electric field (from upstream parameters) is high and the polar cap Pedersen conductivity is high. This is despite the fact that *PCN* is derived by scaling the background subtracted magnetic disturbance ΔF in terms of the same electric field estimate. Figure 1 of Nagatsuma (2004) shows that for large values *PCN* is roughly half what a linear relationship would predict. Hence, despite it being constructed to remove conductivity effects, it appears the PCI do depend on ionospheric conductivity. This means that, if the saturation effect is real and not an artefact of the regression technique, we should also expect to see dipole tilt dependent differences between *PCS* and *PCN*.

1.5 Northward IMF conditions

The other important class of effects causing different responses in *PCN* and *PCS* occur when the IMF has a northward component. Figure 3 shows schematics of potential reconnection sites at the sunward edges of the tail lobes when the IMF points northward and looks at the potential roles of the dipole tilt and the IMF B_X component (Lockwood & Moen, 1999).

The top row is for IMF $B_Z > 0$ and $B_X = 0$. Parts (a) and (c) show that the likely lobe reconnection sites are in the summer hemisphere. This is lobe "stirring" reconnection that causes a circulation cell or cells in that hemisphere and reconfigures the open field lines but does not change the total open flux. This lobe circulation can sometimes be fast and fill the whole polar cap (Q.-H. Zhang et al., 2021). Part (b) shows the more symmetrical situation around the equinoxes with $B_X = 0$. In this case, lobe reconnection could occur in either or both hemispheres. It is possible that field lines reconnected at the sunward edge of one lobe are never reconnected at the equivalent point in the other, giving lobe "stirring" circulation taking place in both polar caps simultaneously. However, it is more likely that field lines reconnected on the sunward edge of one lobe will, at some time, be reconnected at the other (note that such reconnections taking place simultaneously, rather than sequentially, would be relatively rare): in this case the "dual-lobe" reconnection closes open flux. It has been proposed by Milan et al. (2020) that this is the origin of the "horse-collar" auroral form seen during northward IMF intervals (Hones et al., 1989). Another complication is that the larger offset of the southern magnetic pole from the rotational pole, compared to that for the northern pole (Koochak & Fraser-Smith, 2017; Lockwood & Milan, 2023; Lockwood et al., 2021) may make the relative contribution of dipole tilt to the behaviour more important in that hemisphere.

The second row of Figure 3 looks at equinox conditions and shows how $B_X > 0$ (part d) favours lobe reconnection in the southern hemisphere whereas $B_X < 0$ (part f) favours it in the northern. The bottom row looks at the dipole tilt effect for $B_X < 0$. The main point is that for the December solstice this may promote dual lobe reconnection or may just result in reconnection with neither lobe.

From satellite data on F-region ionospheric flows Crooker and Rich (1993) and Rich and Hairston (1994) argued that lobe reconnection was almost entirely the "stirring" form in the summer lobe. Subsequent surveys of more data and better distribution of orbit paths found that summer lobe stirring reconnection, giving sunward flow in part of the polar cap, was dominant but that winter hemisphere lobe reconnection was possible, albeit less common and usually weaker (Weimer, 2001). This was also reported by surveys from the SuperDARN radars (Pettigrew et al., 2010; Ruohoniemi & Greenwald, 2005; Sundberg et al., 2009; Thomas & Shepherd, 2018) but there are complications introduced in these HF radar studies by the relative lack of echoes in the winter hemisphere and the fact it is harder them to access all areas because of propagation path issues. A less-strong summer dominance (but nevertheless a dominance) was reported by Wilder et al. (2009, 2010) whereas Koustov et al. (2017) found a stronger one. Surveys of satellite field-aligned current and flow data also report stronger and more common lobe reconnection signatures in the summer hemisphere under NBz conditions (Reistad et al., 2019, 2021). Lobe reconnection in the winter hemisphere during northward IMF has also been observed using red-line auroral emissions in the cusp region (Lockwood & Moen, 1999).

Sunward flow in the polar cap is registered in the PCI as negative values. Nagatsuma (2002) found negative PCN values required northward IMF and were most common during summer at around 17 h UT. Sunward flows were also found to be more common in summer for PCS by Lukianova et al. (2002). These authors also reported that frequently PCN and PCS had opposite polarities. However they attributed the differences to ionospheric conductivity differences rather than the occurrence of lobe-stirring reconnection predominantly in the summer hemisphere.

From the above discussion, there are a number of physical reasons to expect PCN and PCS to differ. This list is not complete. For example, Troshichev and Janzhura (2012) note that the PCI also correlate with auroral electrojet indices and so conductivity differences associated with hemispheric asymmetries in precipitation in substorm expansion phases.

Section 2 studies the relationship of the two hemispheric polar cap indices to help quantify and understand the differences.

2 Comparison of Northern and Southern Hemisphere Indices

This paper employs the PCI data for both hemispheres, for 1 January 1998 to 31 December 2018 (i.e., 1998-2018, inclusive) that are available from ISGI. The data were downloaded on 11 February 2023 as annual ASCII files. For these years the data for both hemispheres are classed as "definitive" by ISGI. There are also data for 2019-2021 available from ISGI, with the *PCN* data classed as definitive for 2019 and 2020 and "provisional" for 2021 and the *PCS* classed as provisional. The entire study presented here was repeated including these three years (i.e. for 1998-2021, inclusive) and results were extremely similar to those reported here: in addition to sample numbers being greater, correlations were slightly enhanced, significances of correlations considerably enhanced and root-mean-square (r.m.s.) differences between *PCN* and *PCS* very slightly reduced by the inclusion of data for 2019, 2020 and 2021.

One technical detail is that a number of the *PCS* data records have a rogue 99999.00 added to the minutes field. These records are here treated as bad data. In addition, some other records are missing in the *PCS* data series, including all data for 2003. As a result, the 1998-2018 (inclusive) dataset contains 11,028,946 1-min *PCN* samples, and 10,337,662 1-min *PCS* samples out of a possible 11,044,800. The number of simultaneous *PCN* and *PCS* samples is 10,337,561. Note that of the 707,138 missing samples in the *PCS* data, 525,600 are accounted for by the 2003 datagap and 181,538 (in total just over 126 days) are due to the badly-formatted records (with the added 99999.00) and other small datagaps. For *PCN* there are just 15854 missing samples (a total of just over 11 days).

As mentioned above, there have been a considerable number of different versions of the Polar Cap Indices generated and we here define the one used by the source (ISGI), the format (1-year ASCII files generated using the ISGI webpage), the ISGI classification ("definitive") and the date of download (11 February 2023). As also mentioned, there has been debate about the voracity of the PCI data, even after the IAGA endorsement in 2013: this paper takes the data currently available from ISGI at face value and considers interpretation in terms of known mechanisms and physics rather than faulty data or incorrect processing. Of course, some such errors will almost certainly be present in the data, but one aim of this study is to assess how often they are really a factor and how often it is the expectation that they should be the same at any one time that is in error.

Figure 4 compares the occurrence of *PCN* and *PCS* in a 2-dimensional histogram format (hereafter referred to as a 'data density plot'). This is essentially a scatter plot but does not result in loss of information when data pairs are so numerous that points are massively over-plotted on top of each other. Given we here are dealing 10,337,561 valid data pairs at τ=1min, this is a vital consideration. In Figure 4 the number N of simultaneous *PCN* and *PCS* samples are colour coded in bins of *PCN* (the vertical axis) and *PCS* (the horizontal axis) that are 0.5 mVm^{-1} by 0.5 mVm^{-1} in size. Because the range in N is so large (from zero to 10^6) N is coloured on a logarithmic (base 10) scale. On each plot the mauve dashed lines show *PCN=PCS* (the diagonal line), *PCN=0* (the horizontal line) and *PCS=0* (the vertical line).

Figure 4a is for the raw data (averaging timescale τ=1min), for which there are a total of ΣN =10,337,561 samples. Figure 4b is for independent one-hour means (τ=1hr), where 54 one-minute samples in the hour (90%) are required to form a valid mean. This generates ΣN =171,253 samples. Table 2 gives the correlation coefficients, r the probability of the null result that there is no correlation and the r.m.s. deviation $\Delta_{rms} = [\langle (PCN - PCS)^2 \rangle]^{0.5}$. The Table also gives the results for τ=1day, τ=1yr and for all

Table 2. Relationship of *PCN* to *PCS*.

parameter		τ=1min	τ=1hr	τ=1day	τ=1yr	τ=24yr
number of samples	ΣN	10,321,808	171,253	6707	20	1
linear correlation	r	0.787	0.831	0.930	0.939	-
probability of $r = 0$	p	$< 10^{-20}$	$< 10^{-20}$	$< 10^{-20}$	$8.1{\times}10^{-9}$	-
r.m.s difference	Δ_{rms} (mVm^{-1})	0.9015	0.7169	0.3190	0.0669	0.0037

$^{a}\Delta_{rms} = [\langle(PCN - PCS)^2\rangle]^{0.5}$.

the data (1998-2018), τ=21yrs (although note that, because all PCS data for 2003 are missing, only 20 values are available). It can be seen that the correlation coefficient rises with increased τ and Δ_{rms} decreases, as expected. The very small value of Δ_{rms} =0.0037 mVm^{-1} for the overall means and the very high correlation for annual means r=0.939 show that there is almost no systematic difference between PCN and PCS. In addition the quantile-quantile ("q-q") plots in parts (a) and (b) of Figure 4 are very close to straight lines along the diagonal. This shows that the distributions of PCN and PCS values are almost identical. The only difference is a slight deviation from the diagonal seen for the smallest 1% of values (which are negative). This will be interpreted in Section 7.

Table 2 stresses a point that is valid for all comparisons between terrestrial indices and between them and solar wind coupling functions: that the behaviour varies with averaging timescale, τ. In this paper, we study the indices at the raw resolution at which they are published (namely 1 min) and also at one hour, the latter allowing comparisons with the SuperDARN transpolar voltage dataset of Lockwood and McWilliams (2021b). Note that behaviour at intermediate timescales may not be a linear interpolation between the two and almost certainly would not be a linear extrapolation to timescales greater than an hour.

Troshichev et al. (2022b) have looked at differences between PCN and PCS on daily and monthly averaging timescales. They found there were some systematic seasonal differences with values being higher in the summer polar cap for both indices.

The data density plot in Figure 4a shows the good correlation between PCN and PCS (r= 0.787) for positive values, albeit with considerable scatter. However, the agreement of the two is very poor for negative values, for which very few samples align along the diagonal line. Instead there are two populations: one with $PCN < 0$ and $PCS =$ 0 (aligned with the vertical dashed line) and the other with $PCS < 0$ and $PCN = 0$ (aligned with the horizontal dashed line). Figure 4b shows the same features with reduced scatter.

Parts (c) and (d) give important detail by repeating part (a) for 6 months around summer solstice in the Northern hemisphere ($0.216 < F < 0.726$, Figure 4c) and 6 months around summer solstice in the Southern hemisphere ($F < 0.216$ or $F > 0.726$, Figure 4d). These plots clearly demonstrate that the larger negative PCI values are occurring almost entirely in the summer hemisphere.

Figure 5 investigates the role of the IMF B_X component, suggested in Figure 3. All panels are for $\tau = 1$ min. Parts (a) and (b) are for strongly positive B_X (> 5nT) and (c) and (d) are for strongly negative B_X (< −5nT): (a) and (c) are for 6 months around the June solstice and (b) and (d) are for 6 months around the December solstice. The plot shows that for summer in the northern hemisphere the occurrence of negative PCN is slightly enhanced by negative IMF B_X but reduced somewhat by positive B_X. The converse is true for PCS in summer in the southern hemisphere. This is as predicted by Figure 3 but the effect is weaker than the seasonal effect. Further investigation of the

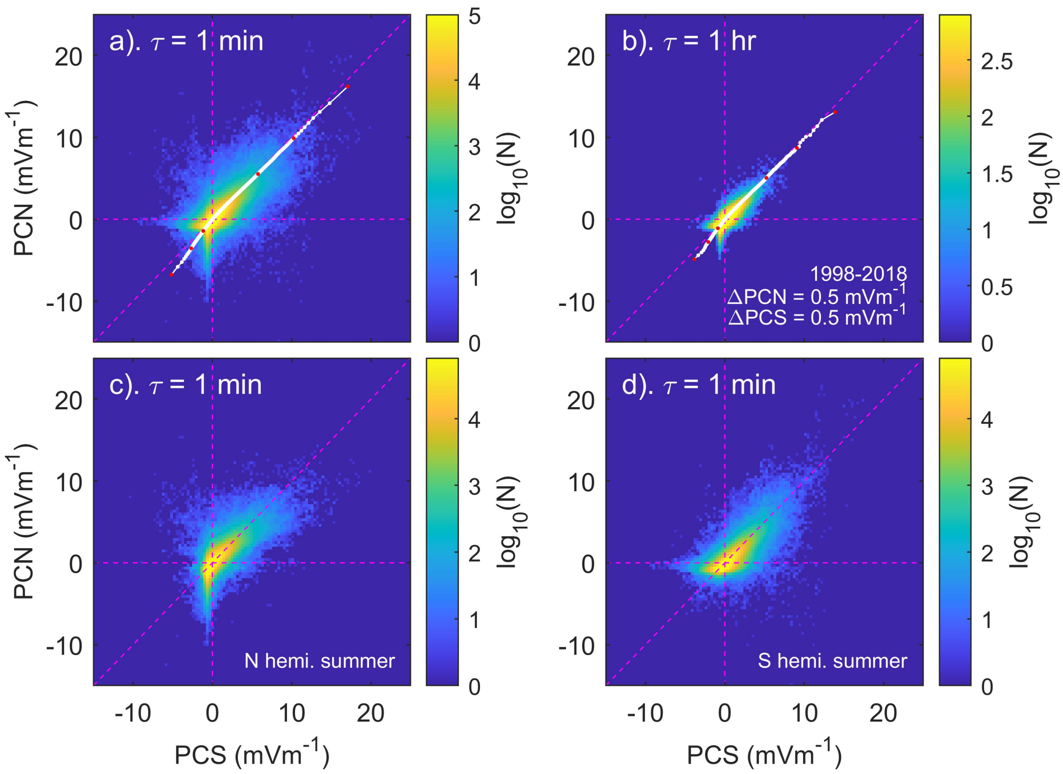

Figure 4. Data density plots (2-dimensional histograms) of *PCN* against *PCS*. The logarithm of the numbers of simultaneous independent samples pairs, N, in bins that are 0.5 mVm^{-1} by 0.5 mVm^{-1} in size are plotted. The data are for 1998-2018, inclusive. (a), (c) and (d) are for the raw 1-minute data; (b) for independent means over intervals τ = 1hr in duration. (a) and (b) are for all data (c) is for six-month intervals around northern hemisphere summer solstice ($0.216 < F < 0.726$) (d) is for six-month intervals around southern hemisphere summer solstice ($F < 0.216$ or $F > 0.726$). Also shown in parts (a) and (b) are q-q plots as white points that are 0.01% apart in quantile level that are joined by a white line and with six points highlighted in red that are the 0.01, 0.1, 1, 99, 99.9 and the 99.99 percentiles).

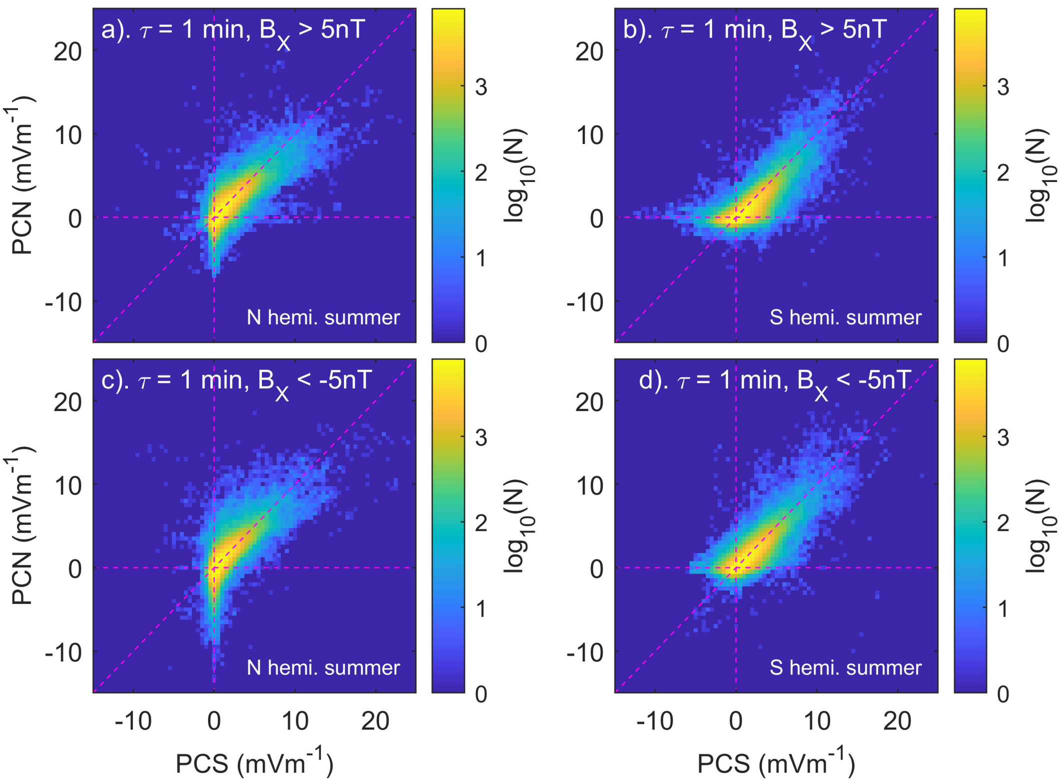

Figure 5. The same format as 4 and for 1-minute data. (a) IMF $B_X > 5$nT and summer in the northern hemisphere; (b) IMF $B_X > 5$nT and summer in the southern hemisphere; (c) IMF $B_X < -5$nT and summer in the northern hemisphere; and (d) IMF $B_X < -5$nT and summer in the southern hemisphere. The seasons are selected using intervals of 6 months around the solstices.

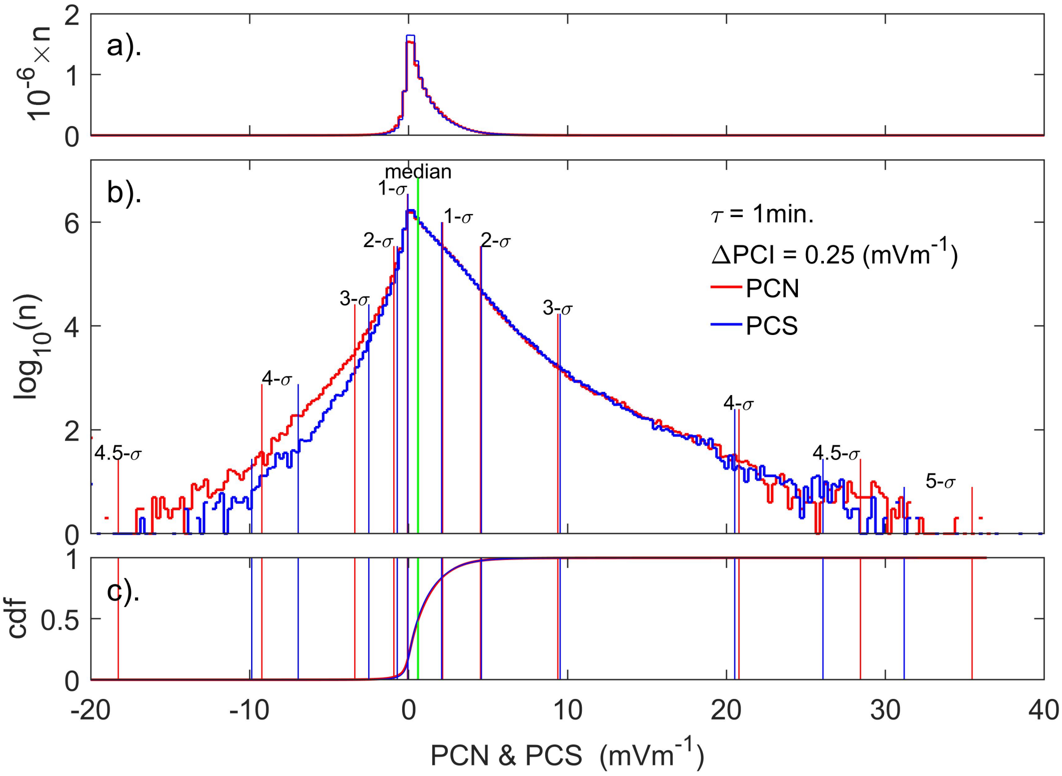

Figure 6. Distributions for the dataset of simultaneous observations of the northern and southern polar cap indices, *PCN* (in red) and *PCS* (in blue). (a) Histogram of the numbers of samples n in bins ΔPCI = 0.25 mVm^{-1} wide, plotted on a linear scale. (b) The same histograms as in part (a), plotted on a logarithmic scale and (c) the corresponding Cumulative Probability Distributions (CDFs). The CDFs are used to define the medians of the distributions and the 1-σ, 2-σ, 3-σ, 4-σ, 4.5-σ and 5-σ points on either side of the median, shown by the vertical lines in parts (b) and (c). Note that in parts (a) and (c) the *PCS* distribution was plotted second in an overlaid thinner blue line to allow some visibility of the *PCN* distribution plotted in a thicker red line.

relative effects of the seasonal dipole tilt and the IMF B_X component will be presented in Section 7.

Figure 6 plots the distributions of simultaneous one-minute samples of *PCN* and *PCS*. The top panel shows the number n of samples in bins 0.25 mVm^{-1} wide on a linear scale. The differences are so small that to give some visibility of both, the *PCN* distribution has been plotted in a thicker red line before being over-plotted with the *PCS* distribution in a thinner blue line. In order to see the small differences between the distributions more clearly, part (b) shows them both on a logarithmic scale. Part (c) shows them as Cumulative Distribution Functions (plotted in the same way as in part (a) because they are so similar) from which the 1-σ to 5-σ points on either side of the median are scaled and are plotted as vertical lines, again in red for *PCN* and blue for *PCS* with the median (which are essentially identical for the two indices) in green.

Part (b) shows the distributions are virtually identical between the -2σ and +4σ points (at -0.68 mVm^{-1} and 20.19 mVm^{-1}) - a range that contains 97.722% of all the samples. In the extreme positive tail of the distributions the number of *PCN* samples is slightly lower than those for *PCS* between the +4-σ and +4.5-σ points but the reverse

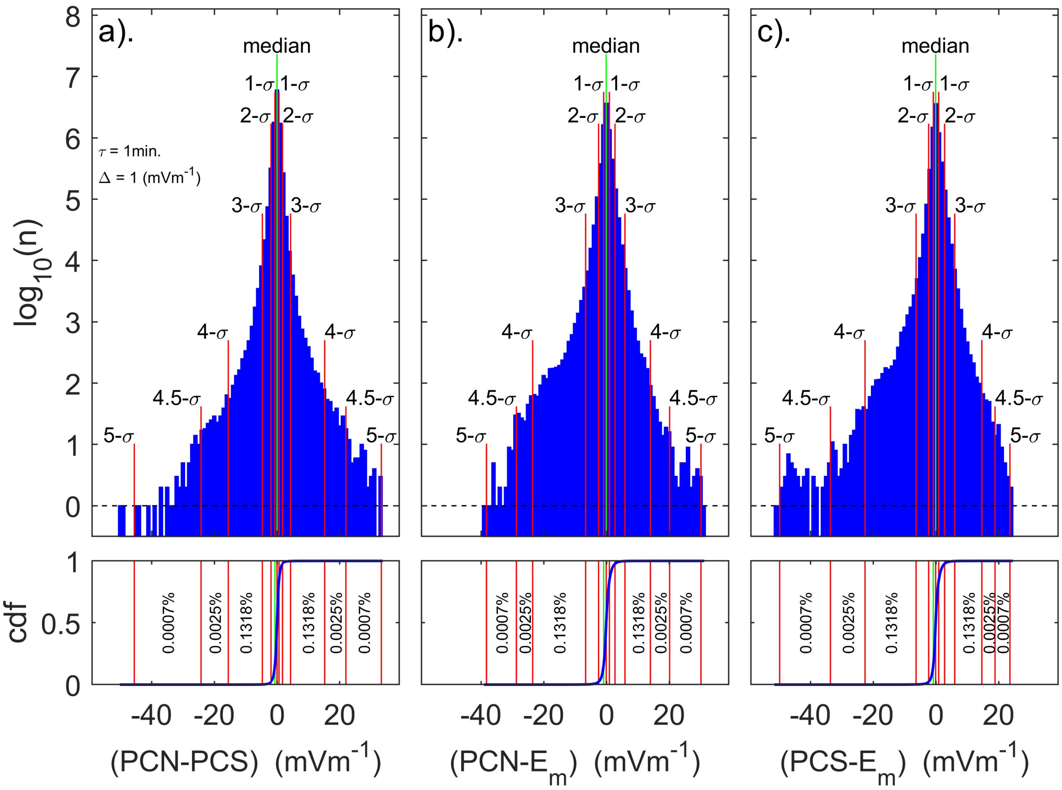

Figure 7. Histogams of the deviation of (a) the northern and southern polar cap indices, $(PCN - PCS)$. (b) the PCN index and the Kan and Lee (1979) estimate of the magnetopause electric field, E_m, $(PCN - E_m)$ and (c) the PCS index and E_m, $(PCS - E_m)$. Histograms are for one-minute values (τ =1 min) and plots give the logarithm to base 10 of the number of simultaneous data points, n, in bins Δ=1 mVm^{-1} wide. The lower panels (c) and (d) show the corresponding cumulative distribution functions (c.d.f.s). The total number of samples is 10,337,561 ($log_{10}(\Sigma n) = 7.01$). The distribution medians are shown by the vertical green lines, and the $\pm 1\sigma$, $\pm 2\sigma$, $\pm 3\sigma$, $\pm 4\sigma$, $\pm 4.5\sigma$, and $\pm 5\sigma$ levels are scaled from the c.d.f.s and plotted in both upper and lower panels as vertical red lines. The horizontal black dashed lines in the upper plots give the one-count level.

Table 3. Parameters of the distributions shown in Figure 7.

level	$(PCN - PCS)$ (mV m^{-1})	$(PCN - E_m)$ (mV m^{-1})	$(PCS - E_m)$ (mV m^{-1})
median	$+0.010$	-0.070	-0.069
$-(1\sigma)$	-0.650	-0.891	-0.819
$+(1\sigma)$	$+0.610$	$+0.937$	$+0.910$
$-(2\sigma)$	-1.870	-2.503	-2.301
$+(2\sigma)$	$+1.700$	$+2.728$	$+2.777$
$-(3\sigma)$	-4.450	-6.637	-6.310
$+(3\sigma)$	$+4.184$	$+5.902$	$+6.013$
$-(4\sigma)$	-14.880	-23.520	-22.582
$+(4\sigma)$	$+14.730$	$+14.005$	$+14.652$
$-(4.5\sigma)$	-23.569	-28.713	-33.612
$+(4.5\sigma)$	$+21.582$	$+20.132$	$+18.860$
$-(5\sigma)$	-44.944	-38.237	-49.795
$+(5\sigma)$	$+33.198$	$+30.125$	$+23.607$

is true for between +4.5-σ and +5-σ. These small deviations of the two distributions in the large positive tail involve only 0.003% of the samples. For the negative PCI tail (sunward convection which is a northward-IMF phenomenon) there is a clear difference between the two distributions below the -2-σ point. This is 2.275% of the samples for which large negative *PCS* is rarer than large negative *PCN*. From Figure 6 we can conclude that for positive values the distributions for *PCN* and *PCS* are essentially identical with some minor differences in only the extreme values (the largest 0.003%), however for negative values there are larger differences and systematic differences that are apparent at larger negative values and involve 2.275% of all samples. Hence the *PCS* index is slightly less good at detecting sunward flow than *PCN*, this is the opposite of what we might expect because of the *MLT* variation of the stations (as discussed in Section 1.1) but could be related to the difference in geomagnetic latitudes for an eccentric field model. The fact that the distributions of *PCN* and *PCS* are essentially identical for the remaining 97.725% of samples is evidence that there is no systematic error in the measurement and processing of the two indices and any errors are random noise and so cancel out.

Figure 7a shows histograms of the differences between simultaneous northern and southern PCI values, *(PCN-PCS)* for the raw 1-minute data. Because the distributons on a linear scale are so similar (as in Figure 6a) we show only the logatithmic histograms so the number in a given bin (in this case of width 1 mVm^{-1}), n, is plotted on a logarithmic scale. This logarithmic scale means that 56% of the one-minute samples are in the central bin. The distribution shown in Figure 7a for 1-minute PCI values shows that the magnitude of the difference between *PCN* and *PCS* is below 0.65 mVm^{-1} for 68.3% of the samples, below 1.87 mVm^{-1} for 95.45%, and below 4.45 mVm^{-1} for 99.73%. If errors were distributed equally between *PCN* and *PCS*, this distribution would be symmetric and this is the case to a good approximation out to the 4σ points which covers 99.994% of the dataset. Specifically, the second column of Table 3 shows that the $+4\sigma$ and -4σ points only differ in $|PCN\text{-}PCS|$ by 0.15 mVm^{-1} which is a 1% difference. Outside the 4σ points, some asymmetry is apparent and the $+4.5\sigma$ and -4.5σ points differ in magnitude by 1.99 mVm^{-1} which is a 8.8% difference and the 5σ and -5σ points differ in magnitude by 11.75 mVm^{-1} which is a 30.1% difference. However, note that the tails outside -4σ, -4.5σ and -5σ contain only 766, 164 and 7 samples (respectively 6.33×10^{-3}%, 1.36×10^{-3}%, and 5.73×10^{-5}% of the total).

To gain some information about how *PCN* or *PCS* individually contribute to the differences shown Figure 7a, 7b and 7c give the corresponding histograms of *(PCN-E_m)* and *(PCS-E_m)*, respectively, where E_m is the Kan and Lee (1979) coupling function aimed at predicting the magnetopause electric field from interplanetary observations and which is used to scale both *PCN* and *PCS*. The E_m data series have been lagged by the optimum propagation delay of $\delta t = 19min$ derived in Section 3. These distributions are not symmetrical, both showing a greater tail of negative values when E_m exceeds the PCI in question. However when we compare the levels of *(PCN-E_m)* and *(PCS-E_m)* in Table 3 out to $\pm 4\sigma$, we find they agree quite closely: the $+4\sigma$ points differing in magnitude by 0.65 mVm^{-1} (a 4.5% deviation) and the -4σ points differing in magnitude by 0.94 mVm^{-1} (a 4.0% deviation). Hence this test against the interplanetary coupling function shows no systematic differences between the behaviour of *PCN* or *PCS* for 99.993% of the samples. There are, however, a few "rogue" points. There is an indication in Figure 7b that *PCN* gives a slight excess of points above the $+4\sigma$ level. More noticeable is a clear additional peak in Figure 7c (for *PCS*) below the -4σ level. However, note that these tails contain just 86 samples each.

We conclude that the numbers samples that do not seem to be showing the same general behaviour in *PCN* and *PCS* is extremely low and that for 99.994% of samples there is no evidence for a systematic error in either *PCN* and *PCS*. Nevertheless, Figure 7a shows that they can differ significantly and Figures 7b and 7c show they can also differ significantly from the observed (lagged) interplanetary coupling function, E_m, used to calibrate the indices. This behaviour is expected physically because the induction effects of changing magnetic fields give a curl of the electric field and so decouple the electric fields at any one time on different points of open field lines.

3 Comparison with solar wind coupling functions

The PCI indices are generated using the regression with the coupling function by Kan and Lee (1979) which aims to estimate the electric field along the magnetopause reconnection line (the reconnection rate), E_m from interplanetary measurements. However, the study by Ridley and Kihn (2004) found that the polar cap indices actually correlate best with transpolar voltage Φ_{PC} which, on average and neglecting any viscous-like voltage, equals the magnetopause reconnection voltage $\Phi_D = E_m.L_X$ where L_X is the length of the magnetopause reconnection X-line. Hence where E_m is the flux transfer rate per unit length of the X-line from open to closed, Φ_D is the total rate of flux transfer from open to closed. Furthermore, (Troshichev, 2022) proposes that the PCI quantify energy input into the magnetosphere, and so should correlate best with interplanetary coupling functions that predict power input into the magnetosphere. As pointed out by Lockwood and McWilliams (2021a) and (Lockwood, 2022), there is no such thing as a "Universal" coupling function that predicts all aspects of the magnetosphere-ionosphere system and the optimum solar wind coupling function needs to be tailored to what aspect of the magnetosphere-ionosphere-thermosphere system it is aimed at predicting. This section studies coupling functions that best predict the polar cap indices.

The first need is to establish the optimum delay between IMF conditions at the nose of the bow shock (as given by the Omni dataset) and the PCI response. The Omni dataset uses an estimated propagation lag from the the satellite to the nose of the bow shock and it should be noted that this generates problems for 1-minute data as it can mean that some plasma is predicted to overtake other plasma in a way that is not physically possible. This paper evaluates the optimum delay for one-minute lag timescales (the resolution of the raw data) and for running one-hour means of the one-minute data. A wide variety of coupling functions were investigated but this paper describes the results for just three: the predictor of magnetopause reconnection electric field E_m proposed by Kan and Lee (1979) (and used to scale *PCN* and *PCS*); the power input into the magnetosphere estimate P_α proposed by Vasyliunas et al. (1982) and the best fit estimator of mag-

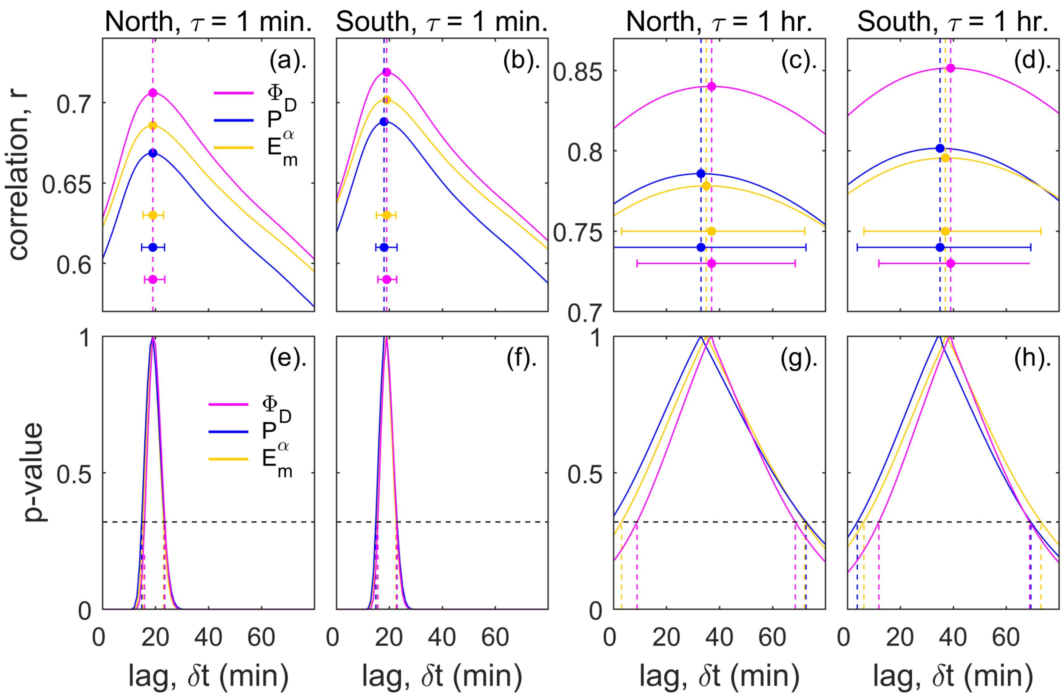

Figure 8. (Top) Lag correlograms (linear correlation coefficient, r as a function of lag δt) between the PCI indices and (mauve) the magnetopause reconnection voltage Φ_D, (orange) the magnetopause reconnection electric field E_m, and (blue) the power input into the magnetosphere P_α, all computed from solar wind parameters. Parts (a) and (b) are for the raw 1-min data and (c) and (d) for running means over intervals of duration τ = 1hr. (a) and (c) are for *PCN* and (b) and (d) are for *PCS*. (Bottom) the corresponding p-values of the null hypothesis that the correlation r at a general lag δt is the same as the peak correlation r_p, computed using the Meng-Z test for the significance of the difference between related correlations (Meng et al., 1992). The horizontal black dashed lines are the 1-σ level which are used to define the uncertainty in the optimum lag, shown by the error bars in the top panels.

netopause reconnection voltage Φ_D derived by Lockwood and McWilliams (2021a). The formula for E_m is given in Equation 2. P_α is given by

$$P_\alpha = B^{2\alpha}(m_{sw}N_{sw})^{(2/3-\alpha)}V_{sw}^{(7/3-2\alpha)}sin^4(\theta/2) \tag{3}$$

where α is the "coupling exponent" which Lockwood (2019) found to be 0.36. The voltage coupling function is

$$\Phi_D = B^{0.643}(m_{sw}N_{sw})^{0.018}V_{sw}^{0.552}sin^{2.5}(\theta/2) \tag{4}$$

The top row of Figure 8 shows the lag correlograms and marks the peak correlation r_p at a lag δt_p with vertical dashed lines. The bottom row shows the probability p that the correlation is the same as the peak value. This is derived using the Meng-Z test for the difference between correlations for inter-correlated parameters (Meng et al., 1992), which is used to derive the uncertainty in the best lag. This test gives the probability that the correlation between A and B is different from the correlation between A and C, allowing for the correlation between B and C and the autocorrelation (ACF) of A. In the present application, it tests the significance of the difference between the peak correlation r_p (at lag δt_p) and that at a general lag δt, r, allowing for the correlation between the time series at lags δt_p and δt and the acf of the PCI time series. The vertical dashed lines in parts (e)-(h) show where p falls below the 1-σ level beyond which r can be considered significantly different to r_p. This gives the uncertainty bars on δt_p shown in parts (a)-(d). For the one-minute data $\delta t = 19 \pm 4$ min applies to all three parameters. For the 1-hour averages the correlograms are much flatter and so the uncertainties in δt_p are much greater: the optimum lags are given in Table 4. This paper employs the given optimum lags for τ=1hr but we should note their large uncertainties.

Figure 8 shows that, of the three coupling functions, Φ_D correlates best with both *PCN* and *PCS* and that *PCS* gives slightly better correlations than *PCN*. Peak correlation for τ=1 min is at a delay δt_p of about 20 min which is somewhat longer than the 6-8 min expected for response in the dayside magnetopause (typically $5min$ to cross the magnetosheath and $1min$ to propagate down dayside field lines into the cusp ionosphere) and the larger lag shows the PCI respond to changes in flows and electric fields in the central polar cap as the convection pattern responds (Morley & Lockwood, 2005). The correlogram is asymmetric with more persistence after peak response than before it, which is consistent with the PCI also correlating with the lagged nightside auroral activity indices, as does transpolar voltage (Lockwood & McWilliams, 2021b). This also explains why in the hourly averages the response peaks at a lag near $40min$.

Using the optimum lags δt_p for τ= 1 hr, we can generate the data-density plots shown in Figure 9 and the correlation details given in Table 4. For correlation studies at τ= 1 hr, this paper uses independent means of hourly intervals containing >50 one-minute samples (>83%) that have been shifted by the optimum lag δt_p derived in Figure 8 from 1-hour running means. Table 4 also gives the p-value for the null hypothesis that there is no correlation (p_r, which is always below the detection threshold) and the rank order n of the correlation coefficients. The last two columns give the probability, $p_{\delta r_n}$, that the correlation is not significantly lower than the correlation above it in the rank order. That comparison is made between the north and south hemisphere for the same interplanetary coupling function in the first of these two columns and for the different coupling functions in the same hemisphere in the second of the two columns: the correlation compared with is given by the r_p rank number, n, in brackets. The $p_{\delta r_n}$ values are derived using the Meng-Z test, described above.

Table 4 shows that the correlations for all three interplanetary coupling functions are slightly, but significantly, greater for *PCS* than for *PCN* and that for both hemispheres,

Table 4. Comparison of correlations between PCN and PCS with various parameters at $\tau =$ 1hr.

Data	N	δt_p *(min)*	Δ_{rms} (mVm^{-1})	r_p	rank n	p_r	$p_{\delta r_n}$ N-S	$p_{\delta r_n}$ same hemisphere
PCS & Φ_D	58182	39 (+30/-27)	0.79	0.864	1	$< 10^{-20}$	-	-
PCN & Φ_D	55051	37 (+32/-28)	0.84	0.851	2	$< 10^{-20}$	$(1)^a$ 0.032	-
PCS & P_α	58192	35 (+34/-31)	0.89	0.808	3	$< 10^{-20}$	-	$(1)^a$ 0.000
PCN & Φ_{PC}	55051	0	0.85	0.763	4	$< 10^{-20}$	-	$(2)^a$ 0.000
PCS & E_m	58192	37 (+36/-31)	0.90	0.759	5	$< 10^{-20}$	-	$(3)^a$ 0.433
PCN & P_α	55051	33 (+40/-34)	0.95	0.751	6	$< 10^{-20}$	$(3)^a$ 0.027	$(5)^a$ 0.000
PCN & E_m	55051	35 (+37/-32)	0.96	0.746	7	$< 10^{-20}$	$(5)^a$ 0.013	$(6)^a$ 0.577

^{a}rank number n of the correlation compared

the correlation is significantly greatest for Φ_D. The statistical significances of the differences between the correlations for P_α and E_m are low.

Figure 9 shows the linear correlation coefficients are highest for Φ_D because its variation with the PCI is nearly linear. Superposed on the data density plots of the indices as a function of the coupling function are the linear regression fits (the mauve lines) and q-q plots (white points that are 0.01% apart in quantile level and the three red points are the 99, 99.9 and 99.99 percentiles). Such q-q plots compare the distributions of the two parameters: if they have the same distribution shape the points line up along the linear regression line, which is the case for the Φ_D-PCI plots for all but the largest 0.03% of the data in the case of PCN (Figure 9a) and all but the top 0.01% of the data in the case of PCS (Figure 9d). The colour pixels of the data density plot at large values and the highest quantiles of-the q-q plot do show some saturation. This saturation is much greater for the other two coupling functions, which have a larger "heavy tail" compared to the PCI indices. In these cases, the q-q plot departs from the linear regression line, most clearly above the 99.0 percentile. This behaviour, as discussed earlier in Section 1.4, has usually been interpreted as a physical mechanism limiting the terrestrial response. However, it can also be interpreted as showing that the coupling function used is not optimum, not being a linear predictor of the terrestrial response.

For both PCN and PCS the best linear regression is for the hourly means (using the optimum lag of δt_p of 38 min) is

$$\langle \Phi_D \rangle_{\tau=1hr} = 18.862 \times \langle PCI \rangle_{\tau=1hr} + 6.14 \tag{5}$$

where Φ_D is in kV and PCI (either PCN or PCS) is in mVm^{-1}.

4 The effect of averaging timescale, τ

Figure 9 shows that Φ_D is a good linear predictor of both PCN and PCS for averaging timescales of τ= 1 hr. However looking at the equivalent plots for τ= 1 min, a somewhat more complex picture emerges. Figure 10 shows this relationship in three different ways. The left-hand column gives data-density plots, overlaid with a linear regression fit and a q-q plot (as shown in parts (a) and (d) of Figure 8 for τ= 1 hr). As for the 1-hour data shown in Figure 9a and 9d, there is some saturation in the data-density and q-q plots for the 1-min PCI values in Figures 10a and 10d. The quantiles of the q-q plot show the distributions of PCI and Φ_D are different above the second red q-q points for which is for the 99.9 percentile, in other words it only effects the largest 0.1% of the 1-minute PCI values. Note that for both indices, all but this extreme tail of the distri-

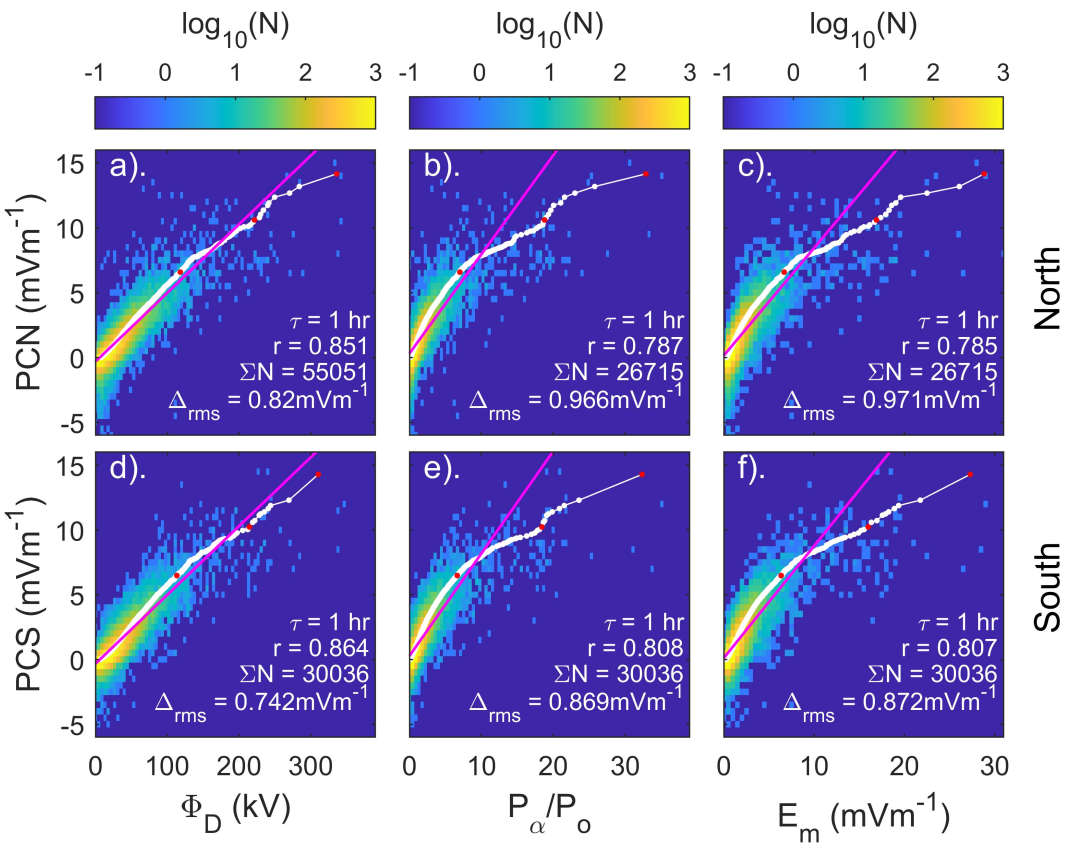

Figure 9. Data density plots (2-dimensional histograms) of hourly means (τ = 1hr) of (top row) PCN and (bottom row) PCN against coupling functions derived from interplanetary observations: (a) and (d) are for the estimated magnetopause reconnection voltage, Φ_D; (b) and (e) are for the normalised estimated power into the magnetosphere P_α/P_o (P_o being the average of P_α over all data); and (c) and (f) are for the predicted merging electric field electric field, $[E_m]$. All interplanetary parameters are lagged by the optimum lags δt_p for τ = 1hr derived from Figure 8. The logarithm of the numbers of simultaneous independent sample pairs, N, are plotted for bins of size that is given in each panel. The mauve line is the best linear least-squares fit to the data. The white dots are q-q plots for quantiles 10^{-4} apart (the points colored red being for the 99, 99.9 and 99.99 percentiles). Also given in each panel is the total number of samples ΣN, the linear correlation coefficient r and the r.m.s. fit residual for the optimum linear regression, Δ_{rms}.

.

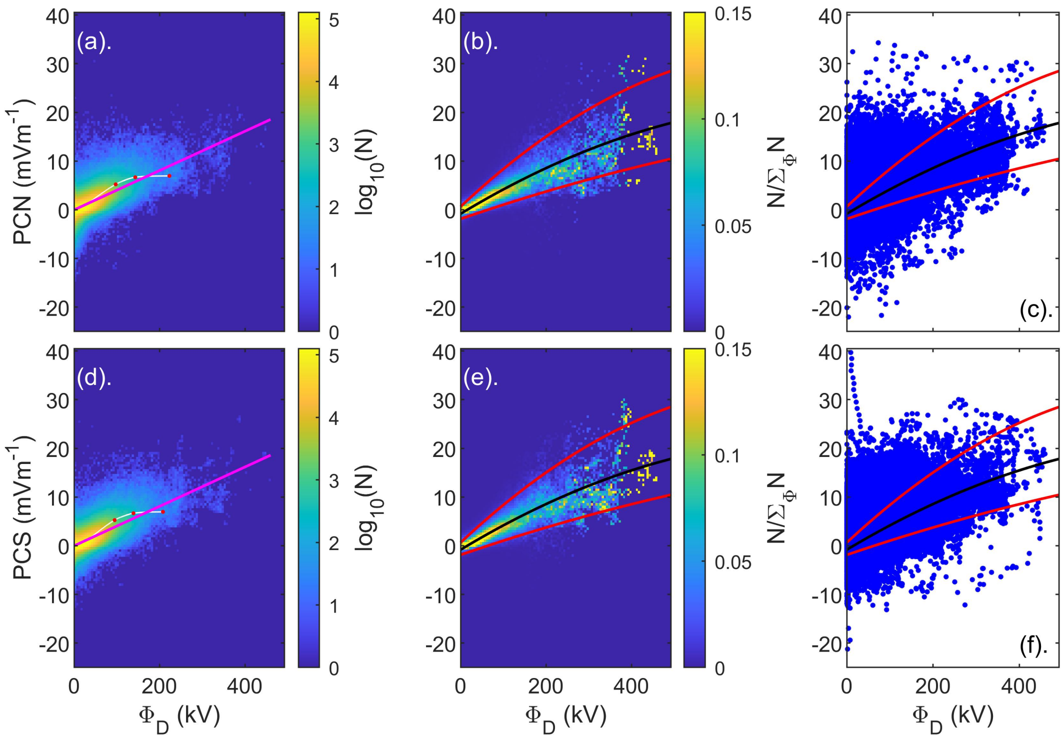

Figure 10. Three ways of studying the relationship at time resolution $\tau = 1$min between the magnetopause reconnection voltage Φ_D, estimated from interplanetary parameters using equation 4, against (top row) PCN and (bottom row) PCS. The optimum lags δt_p, defined by the peak correlations in Figure 8, are used. The data are for 1998-2018. The left hand panels (a) and (d) are data density plots (2-dimensional histograms) of (top) PCN and (bottom) PCS against the predicted reconnection voltage Φ_D . The logarithm of the numbers of simultaneous independent samples pairs, N, is colored in bins that are $\Delta PCB = 0.5$ mVm^{-1} by $\Delta\Phi_D = 0.5$ kV in size. In these panels the white line shows the q-q plot, on which the red points are for the 99, 99.9, and 99.99 percentiles. The mauve line is the least-squares linear regression fit. The middle panels (b) and (e) show the probability density functions (pdf), $N/\Sigma_\Phi N$, where $\Sigma_\Phi N$ is the sum of N for that value of Φ_D. The black line is the best non-linear polynomial fit to the mode values of the pdfs and the red lines are the polynomial fits to the $\pm 1\sigma$ points of the pdfs. The right-hand plots (c) and (f) are scatter plots on which are superposed the same lines as in parts (b) and (e).

bution the variation is very close to linear, but the linear regression line for all data has been pulled to a different slope than applies to 99.9% of the data by the extreme tail of the distribution. The best-fit linear regression is again the same for both PCI:

$$\langle \Phi_D \rangle_{\tau=1min} = 27.413 \times \langle PCI \rangle_{\tau=1min} \tag{6}$$

where, again, Φ_D is in kV and PCI is in mVm^{-1}. The slope is considerably greater because of the saturation effect that limits the PCI values at the largest Φ_D and a linear fit is clearly not ideal.

Parts (b) and (e) of Figure 10 show the same data but instead of colour contouring the (logarithm) of the number of samples in each bin, $log_{10}(N)$ as in parts (a) and (d), they show the probability density in each bin $N/\Sigma_\Phi N$, where $\Sigma_\Phi N$ is the sum of

N over all bins at that value of Φ_D. The black line is a second-order polynomial fit to the mode of these probability density functions (PDFs) and the red lines are fitted to the $\pm 1\sigma$ points of the PDFs.

Parts (c) and (f) of Figure 10 are traditional scatter plots and the fits given in parts (b) and (e) are reproduced. It is immediately apparent there are a lot of data points outside the $\pm 1\sigma$ lines, especially at lower Φ_D values where $\Sigma_\Phi N$ is particularly large. The effect of these outliers can be seen in the data-density plots (a) and (d) but is not as widespread as in the scatter plots because although the colour scale goes right down to the one-count level (N=1, $log_{10}(N)$=0) it does not register single samples in a bin. Hence the scatter plots (c) and (f) tell us about outliers, but nothing about the bulk of the distribution (where the blue data points merge into a blue continuum).

The worst outliers in the scatter plats are in PCS but there are only about 50 of these (out of a total of over 11 million samples). This certainly does not point to a problem with the processing procedure. They are more likely perturbation of the magnetometer observations (for example by a metal object passing nearby) or they could be perturbed by flare- or precipitation-induced conductivity effects. Troshichev et al. (2022b) note that solar proton events cause differences between PCN and PCS implying these particles have access to the polar ionospheren that can be slightly fdifferent in the two hemispheres. Less extreme outliers are seen in both PCS and PCN but there is a difference as for PCN they tend to be at the largest index values whereas for PCS they are symmetrically at the largest and lowest index values.

The second-order fits give the following formulae for the optimum Φ_D and the upper and lower $1\!-\!\sigma$ limits, $[\Phi_D]_{hi}$ and $[\Phi_D]_{lo}$. The fits are valid for one-minute data with $-2 \leq PCI \leq 20$ mVm^{-1}.

$$\Phi_D = 860 - 180 \times (22 - PCI)^{1/2} \tag{7}$$

$$[\Phi_D]_{lo} = 785 - 138 \times (33 - PCI)^{1/2} \tag{8}$$

$$[\Phi_D]_{hi} = 1450 - 310 \times (20 - PCI)^{1/2} \tag{9}$$

where, Φ_D is in kV and PCI (either PCN or PCS) is in mVm^{-1}.

The equivalent plots to Figure 10 were generated for P_α and for $[E_m]$ at $\tau = 1$ min resolution and they show same sort of the behaviour, as would be expected from the plots for $\tau = 1$ hr in Figure 9, other than the saturation effect is greater and sets in at lower values than for Φ_D. Non-linear saturation effects between the E_m coupling function and various versions of PCI have been reported in the past (for example Matzka & Troshichev, 2014; Troshichev et al., 2006; Vennerstrøm, 2019) and has been attributed to incorrect calibration parameters (Stauning, 2018). The present paper is aimed at discussing the differences between the current versions of PCN and PCS published by ISGI and not if, nor how, the scaling and calibration of both could be improved. Hence the key point emphasised here is that Figures 7, 9 and 10 all show the same behaviour for PCN and PCS. On that point, a procedure for generating interplanetary coupling functions tailored to a given terrestrial disturbance measure and that was designed to maximise linearity (and so minimise saturation), has been developed by Lockwood and McWilliams (2021a) and Lockwood (2022) from the analysis initially presented by Vasyliunas et al. (1982) in their development of P_α. This could be applied to the PCI: such work is beyond the scope of the present paper but should be carried out.

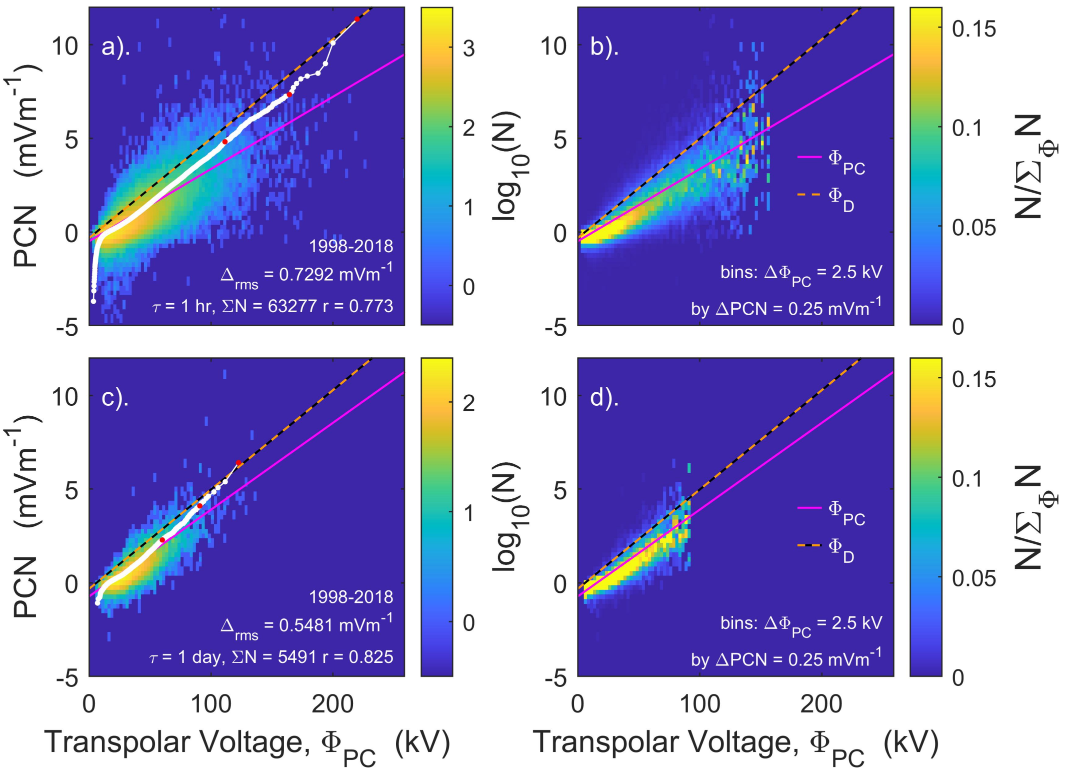

Figure 11. The left-hand panels are data density plots (2-dimensional histograms) of PCN and against the transpolar voltage derived from the northern hemisphere SuperDARN radar array Φ_{PC} from the survey of 25 years of observations by Lockwood and McWilliams (2021b). The logarithm of the numbers of simultaneous independent samples pairs, N, in bins that are ΔPCN = 0.25 mVm^{-1} by $\Delta\Phi_{PC}$ = 2.5 kV in size are plotted. (a) is for τ = 1hr, (b) is for τ = 1day. The mauve line is the best linear regression and the white dots show the q-q plot with quantiles 10^{-4} apart, and the red points are for the 99, 99.9, and 99.99 percentiles. The total number of samples ΣN, the linear correlation coefficient r and the r.m.s. fit residual for the optimum linear regression, Δ_{rms} are given in each case. The black and orange line is the magnetopause reconection voltage Φ_D predicted from PCN using Equation 5. The right-hand panels are the corresponding pdf plots.

5 Relationship with transpolar voltage

This section studies the relationship of hourly means of PCN with the simultaneous transpolar voltage derived from the northern-hemisphere SuperDARN radars using the map-potential technique. The dataset of 1-hour integrations from 25 years of data by Lockwood and McWilliams (2021b) is employed. This section will also look at the effect of further averaging using daily means. The results are shown in Figure 11. It is clear that here is a strong relationship between the two (the correlation coefficient is 0.763). However, the q-q plot shows, it is complex, particularly at low transpolar voltages.

This is to be expected because the transpolar voltage measurements of (Lockwood & McWilliams, 2021b) take the largest potential difference, irrespective of where the maximum and minimum of the potential pattern are. That means that a northward-IMF lobe reconnection potential would be a positive Φ_{PC} but would give negative PCN and this would explain the behaviour of the q-q plot at low values. It also influences the linear

Table 5. Relationship of PCN to northern-hemisphere transpolar voltage Φ_{PC} from the SuperDARN radar network

parameter		τ (hr)		
number of samples	N	1	64393	
linear correlation	r	1	0.763	
probability of $r = 0$	p	1	0	
regression slope	s	1	0.0379	$\mathrm{mVm^{-1}/kV}$
regression intercept	c	1	0.4788	$\mathrm{mVm^{-1}}$
r.m.s fit difference	Δ_{rms}	1	0.7382	$\mathrm{mVm^{-1}}$
regression slope	s'	1	15.372	$\mathrm{kV/mVm^{-1}}$
regression intercept	c'	1	22.866	kV
r.m.s fit difference	Δ'_{rms}	1	14.875	kV
number of samples	N	24	5648	
linear correlation	r	24	0.822	
probability of $r = 0$	p	24	0	
regression slope	s	24	0.0456	$\mathrm{mVm^{-1}/kV}$
regression intercept	c	24	0.7175	$\mathrm{mVm^{-1}}$
r.m.s fit difference	Δ_{rms}	24	0.5445	$\mathrm{mVm^{-1}}$
regression slope	s'	24	14.799	$\mathrm{kV/mVm^{-1}}$
regression intercept	c'	24	22.805	kV
r.m.s fit difference	Δ'_{rms}	24	9.804	kV

$^{a}PCN = s\Phi_{PC} + c$; ^{b} $\Phi_{PC} = s'PCN + c'$.

regression fit to some extent (mauve line) and is one reason why it predicts a higher Φ_{PC} than the predicted Φ_D at a given *PCN*. However, this is not the only reason because Figure 11b shows that the peaks of the pdfs are at a consistently greater Φ_{PC} than the best-fit Φ_D. Away from the negative *PCN* values, the q-q plot is highly linear, showing Φ_{PC} and *PCN* have matching distributions, just as its linearity in Figure 9a shows Φ_D and *PCN* have matching distribution forms for most of the distribution. The difference between the fitted Φ_{PC} and Φ_D at a given *PCN* grows with activity level and so may show the effect of increased nightside reconection voltage Φ_N on *PCN*, consistent with the observations that the PCI correlate with auroral electrojet indices. This could be the case because avaraging over a timescale of τ of one hour is not sufficient to generate steady state (for which $\Phi_N = \Phi_D$). Parts (c) an (d) of Figure 11 show that the difference between the predicted Φ_D and Φ_{PC} at a given *PCN* is reduced for τ of one day, but is still not zero. The correlations and linear regressions between between Φ_{PC} and *PCN* at averaging timescales of one hour and one day are given in Table 5.

Because of the complication of *PCN* having both polarities, whereas Φ_{PC} is only positive, Figure 11 was regenerated using only positive values of *PCN* (not shown). In addition, because the coupling function used to scale *PCN*, E_m is also only positive the analysis was also repeated using $|PCN|$ (also not shown). In both cases, the results were almost identical to Figure 11, other than there were no values below $|PCN| = 0$. The reason is the “Cooks distance” (also called “Cooks-D”) factor is very small for the negative *PCN* values and so they do not influence the regression fit or the correlation to a great extent.

6 Dipole tilt effects

Our understanding of variations of geomagnetic activity with Universal Time UT and fraction of the calendar year F (see recent reviews by Lockwood & Milan, 2023; Lockwood, Owens, Barnard, Haines, et al., 2020; Lockwood, McWilliams, et al., 2020; Lockwood, Owens, Barnard, Watt, et al., 2020; Lockwood et al., 2021) requires that such effects are seen in the PCI and that is investigated in this section. A central part of that understanding is the Russell-McPherron effect of the dipole tilt on the magnetopause reconnection rate Φ_D (Russell & McPherron, 1973) and the key to identifying that effect is to sort the data into the two polarities of the Y-component of the IMF in the GSEQ frame of reference (Lockwood, Owens, Barnard, Haines, et al., 2020; Zhao & Zong, 2012). This is done for all the PCN and PCS data in Figure 12. The right-hand panels show the values of Φ_D predicted from the lagged IMF parameters at the time of the PCI data, (c) being for IMF $[B_Y]_{GSEQ} > 0$ and (f) for $[B_Y]_{GSEQ} < 0$. The black contours are the predictions for the idealised demonstration of the Russell-McPherron effect for which $[B_Z]_{GSEQ} = 0$ (i.e., the IMF lies in the solar equatorial plane as it does on average and as predicted by Parker spiral theory). This yields the observed peaks in Φ_D around $10\,UT$ at the September equinox ($F = 0.726$) for $[B_Y]_{GSEQ} > 0$ and around $22\,UT$ at the March equinox ($F = 0.216$) for $[B_Y]_{GSEQ} < 0$.

Both PCN and PCS have fundamentally the same behaviour as Φ_D in that both show these peaks. However, there are some anomalous features. In particular, in both hemispheres the peaks show consistent extensions into the summer hemisphere (the summer solstice is at $F = 0.471$ in the northern hemisphere and at $F = 0.972$ in the southern). Furthermore, that summer solstice peak is either preceded by, or follows, an unusually deep minimum.

Figure 13 is the same as Figure 12, but the data used are restricted for when the IMF is strongly northward (specifically, the lagged $[B_Z]_{GSM}$ component exceeds +3nT). By excluding all data for southward or near-zero, this reveals the features associated with strongly northward IMF. The main remaining features seen are around summer solstice ($F{\approx}0.5$ for PCN and $F{\approx}1$ for PCS) with positive-then-negative PCN and negative-then-positive PCS seen with increasing UT. This behaviour is explained in the discussion Section 7.3. Note that the right-hand column shows that equinox peaks seen in Φ_D have almost completely disappeared for this strongly northward-IMF data subset.

7 Discussion and Conclusions

This paper has studied similarities and differences between the northern and southern polar cap indices and which aspects of solar wind-magnetosphere coupling of which they are good indicators. There are two parts to the question posed by the title of this paper. The first part is "to what extent do the PCN and PCS indices agree?" Given that there are 20 years of simultaneous 1-minute data classed as definitive, a detailed study of these indices allows us to answer this question quantitatively and with some considerable certainty. The second part is "to what extent should they agree?". This part is considerably harder to answer and in this paper is not answered quantitatively. However, there are indications from theory, from global numerical modelling of the magnetosphere-ionosphere system and from comparing both to the E_m coupling function, derived from interplanetary parameters, that is used to scale both PCN and PCS. Hence although this paper has not quantified the level of disagreement we should expect between PCN and PCS it has outlined the physical reasons why we should expect them to differ. These reasons go far beyond the differences in polar ionospheric conductivity that are the most frequently invoked factor. However, consideration of these factors (in particular, induction effects, northward IMF effects and conductivity effects) does suggest that most of the time the differences between PCN and PCS are real and physical in origin. Even some of the largest differences may be physical in origin and due to transient events, such

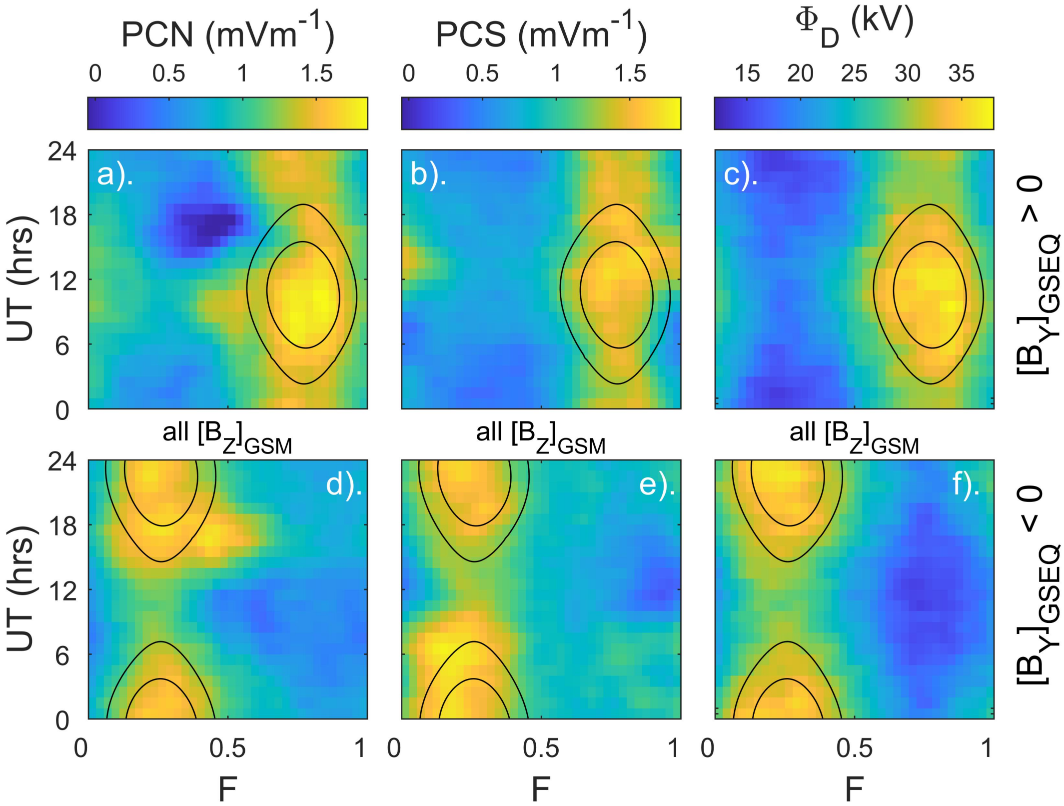

Figure 12. Fraction-of-year (F) - Universal Time UT plots of: (left-hand column) average PCN; (middle column) average PCS and (right-hand column) average Φ_D. The means of all one-minute data are taken in bins that are 1/36 wide in F and 1 hr wide in UT. The upper row is for IMF $[B_Y]_{GSEQ} > 0$ (at the optimum lag before the PCI measurements) the lower row for IMF $[B_Y]_{GSEQ} < 0$. The black lines are two contours of the IMF orientation factor for the simplified demonstration of the Russell-McPherron effect in which the IMF lies in the solar equatorial plane ($[B_Z]_{GSEQ} = 0$). Adapted from Lockwood and Milan (2023).

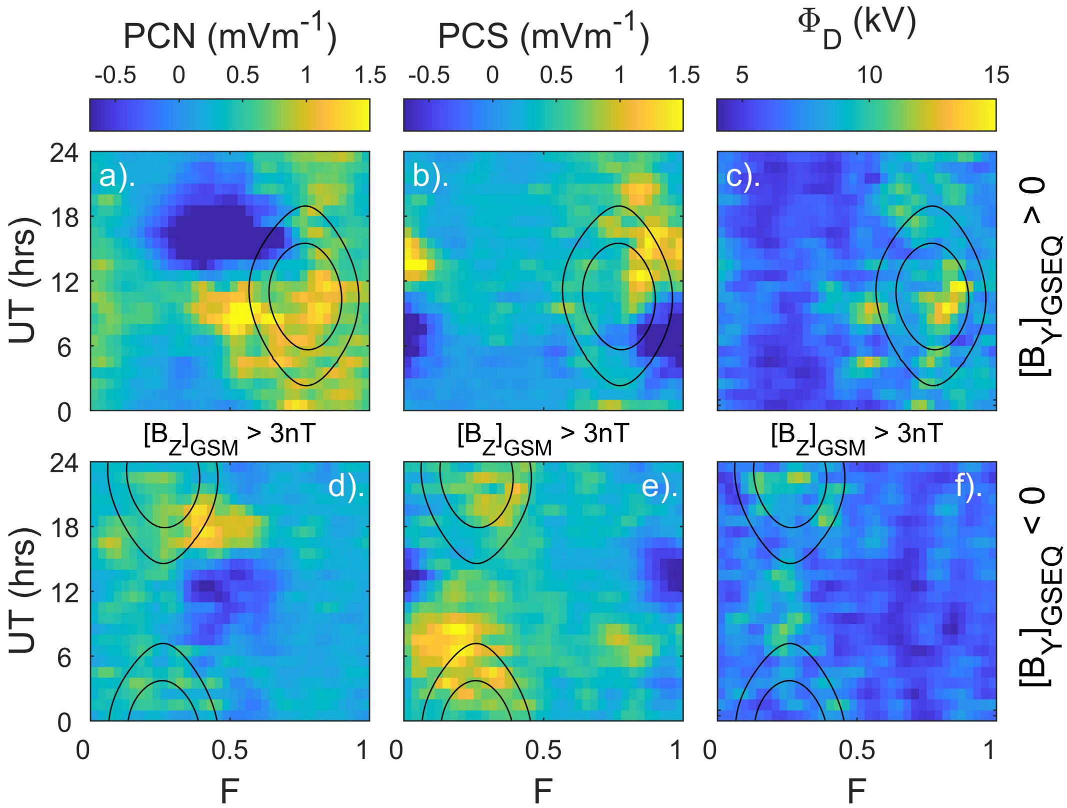

Figure 13. Plot using the same format as Figure 12, but the data used is restricted to times when the lagged IMF $[B_Z]_{GSM}$ component (lagged by the optimum lag of $\delta t = 19\ min$) exceeds $+3nT$.

.

as conductivity enhancement in one polar cap by a large solar flare, but some others could be due to equipment or processing errors. However, the analysis presented does suggest that these are rare.

7.1 Interhemispheric differences

The scatter plots (Figures 10c and 10f) and the distribution of the differences (Figure 7a) show that there are a few one-minute data points of the southern hemisphere index *PCS* that are extreme outliers and an even smaller number of such *PCN* estimates. However, they are minuscule in number (of order 80 out of 11.4 million simultaneous *PCS* and *PCN* samples) and so do not reveal a persistent error in the data processing algorithms. It is recommended that this small number of outliers are studied and either flagged as being caused by an unusual conductivity event (e.g. a solar flare in the summer hemisphere) or are removed if due to an instrumental error.

The overall agreement between the general behaviour of the two indices is excellent and where there are differences between simultaneous 1-minute data they are certainly not larger than we should expect because of induction effects on the field-aligned mapping of electric fields and/or major hemispheric differences in northwarde-IMF reconnection occurrence and rate at the sunward edges of the lobes. For the 1998-2018 (inclusive) period studied, the overall averages of *PCN* and *PCS* agree to within a difference of 0.0043 $\mathrm{mVm^{-1}}$ (0.46% of the overall mean of 0.9464 $\mathrm{mVm^{-1}}$). Table 2 shows how the correlation between *PCN* and *PCS* rises and the rms deviation falls as the averaging timescale τ is increased, as we would expect because of induction effects and temporal variability in the magnetospheric magnetic field.

The quantile-quantile (q-q) plots of *PCN* against *PCS* (parts (a) and (b) of Figure 4) show that they have almost identical distributions. The only exceptions to this are at the lowest 1% of values (which are negative) for which *PCN* shows more large amplitude values than *PCS*. This is the opposite to the expectation from Figure 2 which showed that the rate of change of *MLT* with *UT*, when in the region where sunward convection (negative values) are expected, was lower for Vostok than for Thule, which means Vostok spends longer in that region and should see NBz sunward convection more often then Thule. However, the difference seen in the q-q plots could still be related to the location of the observing sites because, as shown by part (a) and (d) of Figure 1, the two sites differ in the locations relative to the eccentric dipole fields. This spatial difference would matter more for the more localized convection cells inside the polar cap for northward IMF than for the larger scale convection in the polar cap for southward IMF. Another potential source of the difference is the larger offset of the geomagnetic and rotational poles in the Southern hemisphere (Koochak & Fraser-Smith, 2017), which may facilitate lobe reconnection at some times, but make it less common at others. We should also note that the effect is very small and restricted to values below -1 $\mathrm{mVm^{-1}}$. Nevertheless, there are 223314 1-min samples below this level in *PCN* but only 134551 in *PCS*, making strong sunward convection at PCI below this -1 $\mathrm{mVm^{-1}}$ level 40% less common in *PCS* than in *PCN*. It should also be remembered that Figure 4 shows that for positive values the distributions are close to identical. The correlations with solar wind coupling functions are very slightly, but significantly, higher for *PCS* than for *PCN*.

7.2 Induction effects

The effects decoupling the electric fields and voltages that exist simultaneously in the two polar caps are stressed by Figure 7 which shows that the distributions of differences between simultaneous 1-minute values of *PCN* and *PCS* is quite similar to the distributions of differences between each and the Kan and Lee (1979) magnetopause reconnection rate estimate coupling function, E_m. Table 5 shows that the distributions of $(PCN - E_m)$ and of $(PCS - E_m)$ are slightly broader than that of $(PCN - PCS)$ which is to be expected, given that E_m will not be a perfect estimate of the actual reconnection rate and because in computing E_m we have used the optimum lag between the interplanetary data and the PC indices, δt, which in reality will vary around its mean value. The asymmetry in Figures 7b and 7c is caused by northward IMF conditions which can yield negative PCN and/or negative PCS, but E_m is always positive and tends to zero for strongly northward IMF.

The inductive decoupling of electric fields has been well demonstrated by ionospheric observations of the effects of southward turnings of the IMF. The response is to make the cusp aurora and dayside open-closed boundary erode equatorward in a geomagnetic frame as much as to drive poleward plasma flow (for example, Lockwood et al., 2006), which means that the voltage appearing in the ionosphere is smaller than that applied at the reconnection X-line. Lockwood et al. (1986) observed the expansion of the enhanced convection following a southward turning away from noon, an effect modelled by Morley and Lockwood (2005) who showed that the delay before peak response was was seen at dawn and dusk (and hence in Φ_{PC}) was of order 12 minutes, consistent with the observed response delay variation with MLT (Lockwood & Cowley, 1988; Saunders et al., 1992). If we add to this the propagation lag to cross the magnetosheath of about 5 min and a field-aligned propagation time down the ionosphere of 1 min, we have a total of 18 min which is very close to the lag $\delta t = 19 min$ between E_m and the PCI that gives optimum correlation. This is also consistent with the survey of transpolar voltages from the SuperDARN radars by Lockwood and McWilliams (2021b) whch yielded $20 min$ lag between Φ_{PC} and IMF southward component at the nose of the bow shock. During the time that the ionospheric response is growing, the magnetopause reconnection voltage Φ_D exceeds Φ_{PC} and the voltages and electric fields are not mapping. This was demonstrated by the recent survey of a whole year of data (2010) by Milan et al. (2021) who showed that although periods of directly-driven reconnection can occur when $\Phi_D \approx \Phi_{PC}$ and the same is true of quiet times, in general there are periods when the open flux F_{PC} is rising when $\Phi_D > \Phi_{PC}$ and when F_{PC} is falling giving $\Phi_D < \Phi_{PC}$ such that the ratio Φ_D/Φ_{PC} can readily vary between about 0.2 and 5, or even more at low values of Φ_{PC}. This explains the similar variability in the ratios of E_m/PCN and E_m/PCS seen in the present study.

An interesting question arises when considering the effect of pole motions. Recent studies by Lockwood and Milan (2023); Lockwood et al. (2021, 2023) have shown that there are inductive effects caused by the diurnal cycle of sunward and antisunward motions of the ionospheric polar caps. For an eccentric dipole model of the field these can cause simultaneous differences in the transpolar voltages Φ_{PC} in the two hemispheres of up to about 50 kV, the prcise value depending on the dawn-dusk diameter of the open field line polar cap. From Equation 7 of the present paper, for a value of Φ_D of 100 kV (so the polar cap voltages differ from this by $\pm 25\%$), this would cause simultaneous PCI values of 2.98 $\mathrm{mVm^{-1}}$ and 5.32 $\mathrm{mVm^{-1}}$ ($\pm 28\%$ of the mean value), but for Φ_D of 50 kV (so the polar cap voltages differ from this by $\pm 50\%$), this would cause PCI values of 0.48 $\mathrm{mVm^{-1}}$ and 2.98 $\mathrm{mVm^{-1}}$ ($\pm 72\%$ of the mean value). However, it is not certain that the pole-motions would register in the PCI data to this extent, the reason being that the magnetometer stations share the diurnal sunward/antisunward motion of the polar cap and also are, essentially, a magnetic field measurement which does not depend on the reference frame. However, if polar cap conductivities were constant, the change in Φ_{PC} would be reflected in the polar cap currents and the deflections that they cause on the ground and so then the hemispheric differences in the PCI indices would be as great as calculated above. Hence the deviation of one polar cap index from the other would be considerable. This is just for the regular diurnal induction effect caused by the motions of the Earth's poles in a geocentric-solar frame. Other induction effects associated with solar wind-magnetosphere coupling, the substorm cycle and IMF B_Y and B_X components could add considerably to this decoupling of the two indices.

7.3 Northward IMF responses

The results from both polar caps show that the response of the indices to lobe magnetopause reconnection is predominantly a phenomenon of the summer hemisphere. This may be an effect of ionospheric conductivity on the sensitivity of the indices to small dusk-to-dawn electric fields or it may be a reflection of the occurrence and voltage of lobe reconnection. Most likely it is a combination of both.

The schematics in Figure 14 help explain the F-UT behaviour for northward IMF shown in Figure 13. The upper diagrams are convection patterns in an MLT-magnetic latitude frame. The red lines in all three diagrams are the ionospheric footpoints of active reconnection sites and in all three cases there is ongoing tail reconnection (voltage Φ_N) slowly shrinking the polar cap: the blue line is the open-closed field line boundary and the orange arrows show its motion as the polar cap shrinks. In part (a) there is no other reconnection taking place. In particular, there is no magnetopause reconnection, either subsolar ($\Phi_D = 0$) nor on the tail lobe magnetopause ($\Phi_L = 0$) and the pattern is as expected for a contracting polar cap by the ECPC model (Lockwood & McWilliams, 2021b; Lockwood et al., 1990). Beneath the pattern is plotted the associated variation in the dawn-to-dusk electric field in the ionosphere, E_Y, as seen by the polar station as it rotates around the geomagnetic pole (the locus shown by the dashed line in the upper panel). This electric field in the polar cap is positive and weak and is greater when the station is near 00 MLT as that is when it is closest to the footpoint of the tail reconnection site that is causing the flow.

In parts (b) and (c) a lobe reconnection site is active ($\Phi_L > 0$): (b) applies to the northern hemisphere for IMF $B_Y > 0$ and to the southern hemisphere for IMF $B_Y < 0$; conversely, (c) applies to the southern hemisphere for IMF $B_Y > 0$ and to the northern hemisphere for IMF $B_Y < 0$. The MLT of the footpoint of the lobe reconnection X-line is shifted by the effect of the IMF B_Y component of the field line mapping in the magnetosphere, as described by Cowley et al. (1991). Once reconnected, the field lines move towards either dawn or dusk under the field line curvature (a.k.a. "tension") force, thois being the Svalgaard-Mansurov effect for northward IMF, as described by Stubbs et al. (2001). The motion of the observing site in MLT means that in (b) positive and then negative E_Y will be seen whereas in (c) negative then positive E_Y will be seen. This is exactly what is seen for summer data in Figure 13. The conclusion is that the polar cap indices are most sensitive to stirring lobe reconnection cells in the summer hemisphere during northward IMF.

7.4 Optimum solar wind coupling function predictor

This paper has defined the optimum lags between the solar wind conditions at the nose of the bow shock and the indices: for 1-minute data this lag is 19 min with a 1-σ uncertainty of ± 4 min. The best correlations of the PCI with interplanetary parameters is with the estimated magnetopause reconnection voltage, Φ_D, derived by Lockwood and McWilliams (2021a) (given by Equation 4. This performs significantly better as a predictor of PCI than the estimated power input into the magnetosphere, P_α proposed by Vasyliunas et al. (1982), or the estimated magnetopause reconnection electric field E_m proposed by Kan and Lee (1979). Note that E_m is used in the derivation of the PCI. However, this does not give it an advantage in the correlation studies because it scales the observed data, but does not change the waveform of the variation which is set by the observations. This also means that there is no need to change the derivation of the PCI to use a different coupling function to E_m.

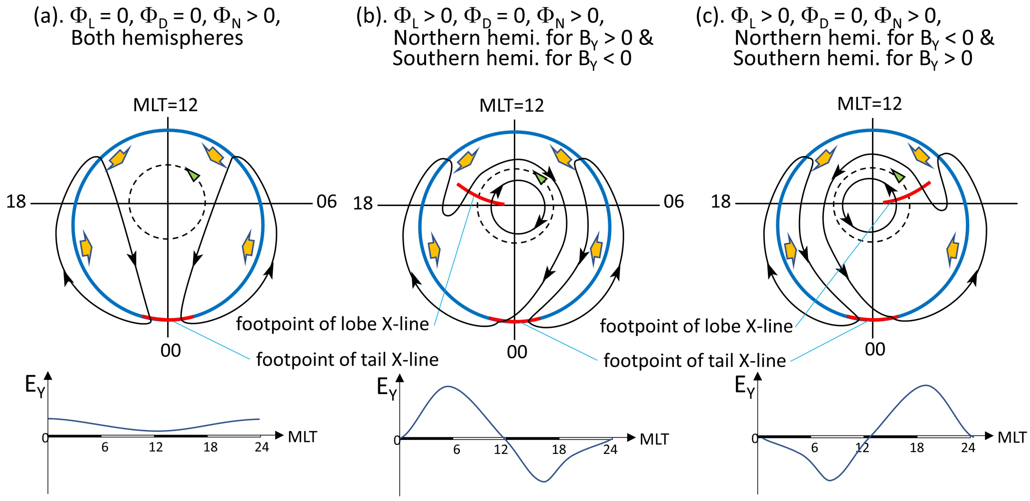

Figure 14. Schematics of convection for northward IMF with no reconnection voltage in the dayside magnetopause (Φ_D=0) but ongoing reconnection in the cross tail current sheet ($\Phi_N > 0$). The polar cap boundary is shown in blue and the polar cap is shrinking as shown by the orange arrows. In part (a) there is no lobe reconnection (Φ_L=0) but in (b) and (c) $\Phi_L > 0$. (b) Applies to the northern polar cap when IMF $B_Y > 0$ and to the southern polar cap when $B_Y < 0$. Conversely, (c) applies to the northern polar cap when IMF $B_Y < 0$ and to the southern polar cap when $B_Y > 0$. Underneath each convection schematic is the variation with MLT of the dawn-to-dusk ionospheric electric field, E_Y, the polarity of which determines the polarity of the polar cap index in that polar cap.

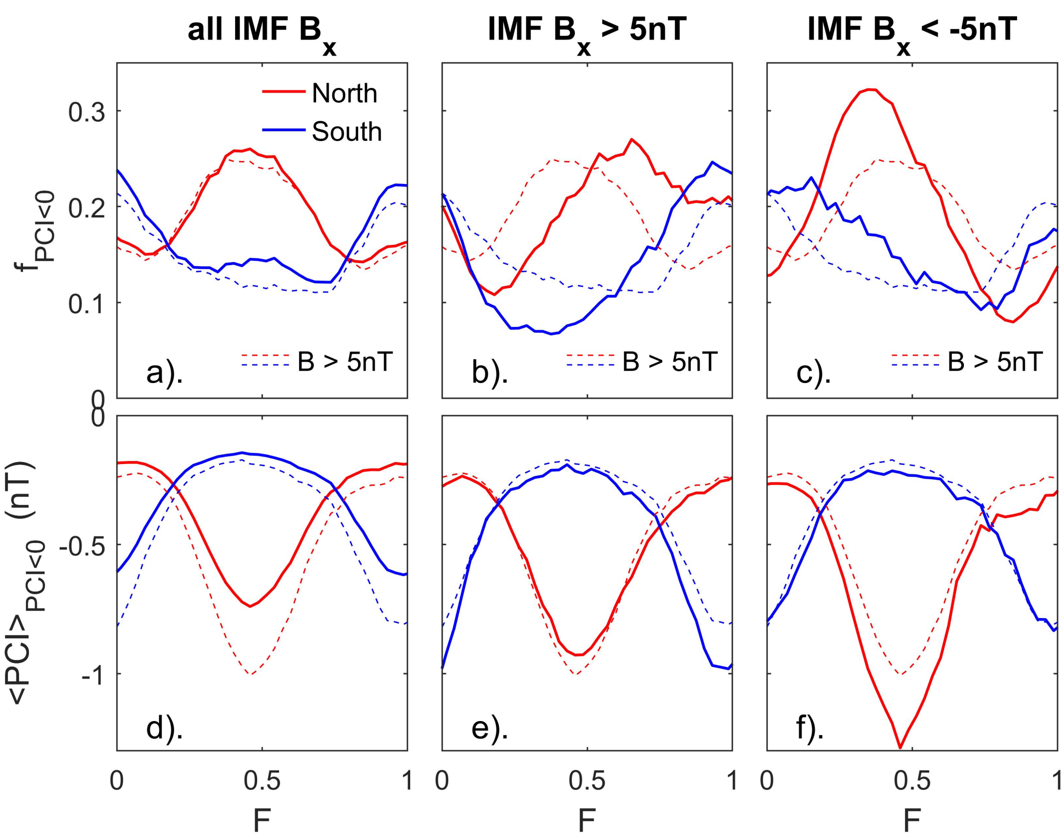

Figure 15. Analysis of the variations with fraction of the calendar year, F of the occurrence and average magnitude of sunward flows in the polar cap, as indicated by negative values of the PCI. The top row (a)-(c) shows the occurrence frequency of negative values, $f_{PCI<0}$ and the bottom row (d)-(f) the mean value of the negative PCI values, $\langle PCI \rangle_{PCI<0}$: red is for the northern hemisphere PCI, *PCN*, and blue for southern, *PCS*. The left-hand column (a) and (d) are for all available samples over the interval 1998-2018, the middle column for when the lagged IMF B_X component exceeds $5nT$ and the right-hand column shows when the lagged IMF B_X is less than -$5nT$. To enable comparisons, the dashed lines in all parts are for all data when the lagged IMF field-strength B exceeds 5nT.

7.5 Dipole tilt and IMF B_X effects

The time-of-year/UT variations of the PCI are dominated by the Russell-McPherron effect on the dayside reconnection voltage. However there are also signatures of lobe reconnection in the summer hemisphere, as discussed above.

Lastly, Figure 15 studies the effects of combinations of time-of-year, F and the IMF B_X component in driving sunward convection, as detected by negative PCI, during northward-IMF conditions, as suggested in Figure 3 and indicated by Figure 5. Figure 15 shows variations with fraction of the calendar year F of the occurrence ($f_{PCI<0}$) and average magnitude ($\langle PCI \rangle_{PCI<0}$) of negative values of the PCI. Red is for the northern hemisphere PCI, *PCN*, and blue for southern, *PCS*.

Parts (a) and (c) of Figure 3 suggest that lobe reconnection giving negative PCI should be most easily facilitated is the summer hemisphere. This is seen to be the case in Figures 15a and 15d. The summer/winter ratio of the occurrence frequencies of negative *PCN*, $f_{PCI<0}$, is about 1.6, and that for negative *PCS* is about 1.4. Larger values are seen in the summer/winter ratio of the means of all the negative values, $\langle PCI \rangle_{PCI<0}$ which is ≈4.0 for *PCN* and ≈3.8 for *PCS*.

The mean negative values are increased at all F by increased IMF magnitude B. This is shown by the dashed lines in Figure 15d which plot the values $\langle PCI \rangle_{PCI<0}$ for the subset of the data with $B > 5nT$. Although the mean negative values are increased in size at all F, they are most increased in summer and the summer/winter ratios are ≈4.9 and ≈5.2 for *PCN* and *PCS*, respectively. Figure 15a shows that the occurrence frequencies of negative flow for $B > 5nT$ are very similar indeed to the values for all data. Thus we can infer that for higher IMF B the occurrence of lobe reconnection is not changed but the voltage of that reconnection is increased. This dependence on the IMF must be a reconnection effect and not associated with the ionospheric conductivities.

Parts (d) and (f) of Figure 3 suggest that lobe reconnection should be enhanced in the Southern hemisphere for positive IMF B_X and should be enhanced in the Northern hemisphere for negative IMF B_X. Figures 15b and 15e are for the data subset with $B_X > 5nT$ and Figures 15c and 15f are for the data subset with $B_X < -5nT$. In each case, the corresponding dashed line for the $B > 5nT$ data subset is reproduced for comparison from Figures 15a and 15d. Figure 15e shows that for *PCN* the variations of $\langle PCI \rangle_{PCI<0}$ for the $B_X > 5nT$ and $B > 5nT$ subsets are almost identical but that for *PCS* the negative values are indeed somewhat enhanced in the summer hemisphere. Correspondingly, Figure 15f shows that the means the negative *PCS* for the $B_X < -5nT$ and $B > 5nT$ datasets are almost identical but the mean negative values in the summer hemisphere for *PCN* are greater in magnitude for $B_X < -5nT$. In both cases the winter values are enhanced by about the same factor as the summer ones and so the summer/winter ratios remain the same at 5 or over. This shows that positive/negative IMF $B_X nT$ does enhance reconnection voltages in the southern/northern hemisphere, as predicted by Figure 3, but the effect is small compared to the summer-winter difference introduced by the dipole tilt. There is no evidence that the reconnection voltage is simultaneously decreased in the opposite hemisphere by the IMF $B_X nT$ component.

The dependence of occurrence of negative values $f_{PCI<0}$ on IMF B_X is rather more complex, as shown in Figures 15b and 15c. For $B_X < -5nT$ (Figure 15c) the occurrence of lobe reconnection is enhanced in northern hemisphere summer but decreased in winter. The same thing is seen For $B_X > 5nT$ (Figure 15b) for the southern hemisphere. However, both hemispheres and IMF B_X polarities show shifts of the peaks and troughs of $f_{PCI<0}$ away from the solstices, unlike the behaviour of $\langle PCI \rangle_{PCI<0}$. We infer that many low-voltage lobe reconnections can occur at a variety of times but these do not greatly influence the mean values of negative PCI which are determined primarily by time-of-year with some effect of the IMF B_X component, as predicted by Figure 3.

Note that for larger IMF magnitudes ($B > 5nT$), the effects of lobe reconnection on the polar cap indices is consistently 5 times greater in the summer hemisphere than in the winter hemisphere. Including all data we find this factor is close to 4 (values of $\langle PCI \rangle_{PCI<0}$ are larger for larger B but the summer/winter ratio is always between 4 and 5. Thus the occurrence and effects of lobe reconnection during northward IMF at the solstices is one significant reason why simultaneous *PCS* and *PCN* do not agree. However, the overall distribution of values of *(PCN-PCS)* shows considerable spread at 1-minute resolution which decreases with averaging timescale and the overall means show that there is no systematic difference between *PCS* and *PCN*. Other differences between simultaneous values at high time resolution are readily explicable because of induction effects that mean that solar wind electric fields do not map down open field lines into the ionosphere, except in long-term averages.

References

Atkinson, G. (1967). An approximate flow equation for geomagnetic flux tubes and its application to polar substorms. *Journal of Geophysical Research*, *72*(21), 5373–5382. Retrieved 2022-11-11, from http://doi.wiley.com/10.1029/JZ072i021p05373 doi: 10.1029/JZ072i021p05373

Atkinson, G. (1978). Energy flow and closure of current systems in the magnetosphere. *Journal of Geophysical Research*, *83*(A3), 1089–1103. Retrieved 2022-11-10, from http://doi.wiley.com/10.1029/JA083iA03p01089 doi: 10.1029/JA083iA03p01089

Baker, K. B., & Wing, S. (1989). A new magnetic coordinate system for conjugate studies at high latitudes. *Journal of Geophysical Research*, *94*(A7), 9139. Retrieved 2023-02-16, from http://doi.wiley.com/10.1029/JA094iA07p09139 doi: 10.1029/JA094iA07p09139

Borovsky, J. E., & Birn, J. (2014). The solar wind electric field does not control the dayside reconnection rate. *Journal of Geophysical Research: Space Physics*, *119*(2), 751–760. Retrieved 2023-04-19, from http://doi.wiley.com/10.1002/2013JA019193 doi: 10.1002/2013JA019193

Borovsky, J. E., Lavraud, B., & Kuznetsova, M. M. (2009). Polar cap potential saturation, dayside reconnection, and changes to the magnetosphere. *Journal of Geophysical Research: Space Physics*, *114*(A3), n/a–n/a. Retrieved 2022-11-10, from http://doi.wiley.com/10.1029/2009JA014058 doi: 10.1029/2009JA014058

Brekke, A., & Moen, J. (1993). Observations of high latitude ionospheric conductances. *Journal of Atmospheric and Terrestrial Physics*, *55*(11-12), 1493–1512. Retrieved 2022-12-09, from https://linkinghub.elsevier.com/retrieve/pii/002191699390126J doi: 10.1016/0021-9169(93)90126-J

Carter, J. A., Milan, S. E., Paxton, L. J., Anderson, B. J., & Gjerloev, J. (2020). Height-integrated ionospheric conductances parameterized by interplanetary magnetic field and substorm phase. *Journal of Geophysical Research: Space Physics*, *125*(10). Retrieved 2022-11-10, from https://onlinelibrary.wiley.com/doi/10.1029/2020JA028121 doi: 10.1029/2020JA028121

Chun, F., Knipp, D., McHarg, M., Lu, G., Emery, B., Vennerstrøm, S., & Troshichev, O. (1999). Polar cap index as a proxy for hemispheric Joule heating. *Geophysical Research Letters*, *26*(8), 1101–1104. Retrieved 2023-02-20, from http://doi.wiley.com/10.1029/1999GL900196 doi: 10.1029/1999GL900196

Connor, H. K., Zesta, E., Ober, D. M., & Raeder, J. (2014). The relation between transpolar potential and reconnection rates during sudden enhancement of solar wind dynamic pressure: OpenGGCM-CTIM results. *Journal of Geophysical Research: Space Physics*, *119*(5), 3411-3429. Retrieved from https://agupubs.onlinelibrary.wiley.com/doi/abs/10.1002/2013JA019728 doi: 10.1002/2013JA019728

Cowley, S. W. H., & Lockwood, M. (1992). Excitation and decay of solar wind-driven flows in the magnetosphere-ionosphere system. *Annales Geophysicae*, *10*, 103–115. Retrieved 2022-08-18, from https://ui.adsabs.harvard.edu/abs/1992AnGeo..10..103C (ADS Bibcode: 1992AnGeo..10..103C)

Cowley, S. W. H., Morelli, J. P., & Lockwood, M. (1991). Dependence of convective flows and particle precipitation in the high-latitude dayside ionosphere on the X and Y components of the interplanetary magnetic field. *Journal of Geophysical Research*, *96*(A4), 5557–5564. Retrieved 2022-08-18, from http://doi.wiley.com/10.1029/90JA02063 doi: 10.1029/90JA02063

Crooker, N. U., & Rich, F. J. (1993). Lobe cell convection as a summer phenomenon. *Journal of Geophysical Research: Space Physics*, *98*(A8), 13403–13407. Retrieved 2023-01-24, from http://doi.wiley.com/10.1029/93JA01037 doi: 10.1029/93JA01037

Gordeev, E. I., Sergeev, V. A., Pulkkinen, T. I., & Palmroth, M. (2011). Contribution of magnetotail reconnection to the cross-polar cap electric potential drop. *Journal of Geophysical Research: Space Physics*, *116*(A8), n/a–n/a. Retrieved 2023-02-23, from http://doi.wiley.com/10.1029/2011JA016609 doi: 10.1029/2011JA016609

Hairston, M. R., Hill, T. W., & Heelis, R. A. (2003). Observed saturation of the ionospheric polar cap potential during the 31 March 2001 storm. *Geophysical Research Letters*, *30*(6). Retrieved 2022-12-09, from http://doi.wiley.com/10.1029/2002GL015894 doi: 10.1029/2002GL015894

Holzer, R. E., McPherron, R. L., & Hardy, D. A. (1986). A quantitative empirical model of the magnetospheric flux transfer process. *Journal of Geophysical Research*, *91*(A3), 3287. Retrieved 2022-11-07, from http://doi.wiley.com/10.1029/JA091iA03p03287 doi: 10.1029/JA091iA03p03287

Hones, E. W. J., Craven, J. D., Frank, L. A., Evans, D. S., & Newell, P. T. (1989). The horse-collar aurora: A frequent pattern of the aurora in quiet times. *Geophysical Research Letters*, *16*(1), 37-40. Retrieved from https://agupubs.onlinelibrary.wiley.com/doi/abs/10.1029/GL016i001p00037 doi: 10.1029/GL016i001p00037

Kan, J. R., & Lee, L. C. (1979). Energy coupling function and solar wind-magnetosphere dynamo. *Geophysical Research Letters*, *6*(7), 577–580. Retrieved 2023-02-25, from http://doi.wiley.com/10.1029/GL006i007p00577 doi: 10.1029/GL006i007p00577

Koochak, Z., & Fraser-Smith, A. C. (2017). An update on the centered and eccentric geomagnetic dipoles and their poles for the years 1980–2015. *Earth and Space Science*, *4*(10), 626–636. Retrieved 2022-10-27, from https://onlinelibrary.wiley.com/doi/10.1002/2017EA000280 doi: 10.1002/2017EA000280

Koustov, A. V., Yakymenko, K. N., & Ponomarenko, P. V. (2017). Seasonal effect for polar cap sunward plasma flows at strongly northward IMF B_z. *Journal of Geophysical Research: Space Physics*, *122*(2), 2530–2541. Retrieved 2023-02-24, from https://onlinelibrary.wiley.com/doi/abs/10.1002/2016JA023556 doi: 10.1002/2016JA023556

Kubota, Y., Nagatsuma, T., Den, M., Tanaka, T., & Fujita, S. (2017). Polar cap potential saturation during the Bastille Day storm event using global MHD simulation. *Journal of Geophysical Research: Space Physics*, *122*(4), 4398–4409. Retrieved 2022-12-09, from http://doi.wiley.com/10.1002/2016JA023851 doi: 10.1002/2016JA023851

Laundal, K. M., & Richmond, A. D. (2017). Magnetic coordinate systems. *Space Science Reviews*, *206*(1-4), 27–59. Retrieved 2023-02-16, from http://link.springer.com/10.1007/s11214-016-0275-y doi: 10.1007/s11214-016-0275-y

Lockwood, M. (2019). Does adding solar wind Poynting flux improve the optimum solar wind-magnetosphere coupling function? *Journal of Geophysical Research: Space Physics*, *124*(7), 5498–5515. Retrieved 2022-08-18, from https://onlinelibrary.wiley.com/doi/10.1029/2019JA026639 doi: 10.1029/2019JA026639

Lockwood, M. (2022). Solar wind—magnetosphere coupling functions: Pitfalls, limitations, and applications. *Space Weather*, *20*(2). Retrieved 2022-05-27, from https://onlinelibrary.wiley.com/doi/10.1029/2021SW002989 doi: 10.1029/2021SW002989

Lockwood, M., & Cowley, S. (1988). Observations at the magnetopause and in the auroral ionosphere of momentum transfer from the solar wind. *Advances in Space Research*, *8*(9-10), 281–299. Retrieved 2022-09-03, from https://linkinghub.elsevier.com/retrieve/pii/0273117788901421 doi: 10.1016/0273-1177(88)90142-1

Lockwood, M., & Cowley, S. W. H. (1992, January). Ionospheric convection and the substorm cycle. In C. Mattock (Ed.), *Substorms 1, proceedings of the first international conference on substorms, ics-1* (Vol. ESA-SP-335, p. 99-109). Noordwijk, The Netherlands: European Apace Agency Publications. (Proceedings of First International Conference on Substorms, ICS-1,held at Kiruna, Sweden on 23-27 March 1992)

Lockwood, M., & Cowley, S. W. H. (2022). Magnetosphere-Ionosphere Coupling: Implications of Non-Equilibrium Conditions. *Frontiers in Astronomy and Space Sciences*, *9*, 908571. Retrieved 2022-08-18, from `https://www.frontiersin.org/articles/10.3389/fspas.2022.908571/full` doi: 10.3389/fspas.2022.908571

Lockwood, M., Cowley, S. W. H., & Freeman, M. P. (1990). The excitation of plasma convection in the high-latitude ionosphere. *Journal of Geophysical Research*, *95*(A6), 7961. Retrieved 2022-08-18, from `http://doi.wiley.com/10.1029/JA095iA06p07961` doi: 10.1029/JA095iA06p07961

Lockwood, M., Haines, C., Barnard, L. A., Owens, M. J., Scott, C. J., Chambodut, A., & McWilliams, K. A. (2021). Semi-annual, annual and Universal Time variations in the magnetosphere and in geomagnetic activity: 4. Polar cap motions and origins of the Universal Time effect. *Journal of Space Weather and Space Climate*, *11*, 15. Retrieved 2022-08-18, from `https://www.swsc-journal.org/10.1051/swsc/2020077` doi: 10.1051/swsc/2020077

Lockwood, M., Lanchester, B. S., Morley, S. K., Throp, K., Milan, S. E., Lester, M., & Frey, H. U. (2006). Modeling the observed proton aurora and ionospheric convection responses to changes in the IMF clock angle: 2. Persistence of ionospheric convection. *Journal of Geophysical Research*, *111*(A2), A02306. Retrieved 2022-08-18, from `http://doi.wiley.com/10.1029/2003JA010307` doi: 10.1029/2003JA010307

Lockwood, M., & McWilliams, K. A. (2021a). On optimum solar wind-magnetosphere coupling functions for transpolar voltage and planetary geomagnetic activity. *Journal of Geophysical Research: Space Physics*, *126*(12). Retrieved 2022-05-28, from `https://onlinelibrary.wiley.com/doi/10.1029/2021JA029946` doi: 10.1029/2021JA029946

Lockwood, M., & McWilliams, K. A. (2021b). A survey of 25 years' transpolar voltage data from the SuperDARN radar network and the expanding-contracting polar cap model. *Journal of Geophysical Research: Space Physics*, *126*(9). Retrieved 2022-08-18, from `https://onlinelibrary.wiley.com/doi/10.1029/2021JA029554` doi: 10.1029/2021JA029554

Lockwood, M., McWilliams, K. A., Owens, M. J., Barnard, L. A., Watt, C. E., Scott, C. J., . . . Coxon, J. C. (2020). Semi-annual, annual and Universal Time variations in the magnetosphere and in geomagnetic activity: 2. Response to solar wind power input and relationships with solar wind dynamic pressure and magnetospheric flux transport. *Journal of Space Weather and Space Climate*, *10*, 30. Retrieved 2022-08-18, from `https://www.swsc-journal.org/10.1051/swsc/2020033` doi: 10.1051/swsc/2020033

Lockwood, M., & Milan, S. (2023). Universal time variations in the magnetosphere. *Frontiers in Astronomy and Space Sciences*, *10*(9), 1139295. Retrieved 2023-02-16, from `https://www.frontiersin.org/articles/10.3389/fspas.2023.1139295/full` doi: 10.3389/fspas.2023.1139295

Lockwood, M., & Moen, J. I. (1999). Reconfiguration and closure of lobe flux by reconnection during northward IMF: possible evidence for signatures in cusp/cleft auroral emissions. *Annales Geophysicae*, *17*(8), 996–1011. Retrieved 2022-08-18, from `https://angeo.copernicus.org/articles/17/996/1999/` doi: 10.1007/s00585-999-0996-2

Lockwood, M., & Morley, S. K. (2004). A numerical model of the ionospheric signatures of time-varying magneticreconnection: I. ionospheric convection. *An-*

nales Geophysicae, *22*(1), 73–91. Retrieved 2022-08-18, from https://angeo.copernicus.org/articles/22/73/2004/ doi: 10.5194/angeo-22-73-2004

Lockwood, M., Owens, M. J., & Barnard, L. A. (2023). Universal Time variations in the magnetosphere and the effect of CME arrival time: Analysis of the February 2022 event that led to the loss of Starlink satellites. *Journal of Geophysical Research: Space Physics*, *128*(3). Retrieved 2023-03-11, from https://onlinelibrary.wiley.com/doi/10.1029/2022JA031177 doi: 10.1029/2022JA031177

Lockwood, M., Owens, M. J., Barnard, L. A., Haines, C., Scott, C. J., McWilliams, K. A., & Coxon, J. C. (2020). Semi-annual, annual and Universal Time variations in the magnetosphere and in geomagnetic activity: 1. Geomagnetic data. *Journal of Space Weather and Space Climate*, *10*, 23. Retrieved 2022-08-18, from https://www.swsc-journal.org/10.1051/swsc/2020023 doi: 10.1051/swsc/2020023

Lockwood, M., Owens, M. J., Barnard, L. A., Watt, C. E., Scott, C. J., Coxon, J. C., & McWilliams, K. A. (2020). Semi-annual, annual and Universal Time variations in the magnetosphere and in geomagnetic activity: 3. Modelling. *Journal of Space Weather and Space Climate*, *10*, 61. Retrieved 2022-08-18, from https://www.swsc-journal.org/10.1051/swsc/2020062 doi: 10.1051/swsc/2020062

Lockwood, M., van Eyken, A. P., Bromage, B. J. I., Willis, D. M., & Cowley, S. W. H. (1986). Eastward propagation of a plasma convection enhancement following a southward turning of the interplanetary magnetic field. *Geophysical Research Letters*, *13*(1), 72–75. Retrieved 2022-08-18, from http://doi.wiley.com/10.1029/GL013i001p00072 doi: 10.1029/GL013i001p00072

Lukianova, R. (2003). Magnetospheric response to sudden changes in solar wind dynamic pressure inferred from polar cap index. *Journal of Geophysical Research*, *108*(A12), 1428. Retrieved 2022-11-11, from http://doi.wiley.com/10.1029/2002JA009790 doi: 10.1029/2002JA009790

Lukianova, R. (2007). Comment on "Unified PCN and PCS indices: Method of calculation, physical sense, and dependence on the IMF azimuthal and northward components" by O. Troshichev, A. Janzhura, and P. Stauning. *Journal of Geophysical Research: Space Physics*, *112*(A7), n/a–n/a. Retrieved 2023-02-20, from http://doi.wiley.com/10.1029/2006JA011950 doi: 10.1029/2006JA011950

Lukianova, R., Troshichev, O., & Lu, G. (2002). The polar cap magnetic activity indices in the southern (PCS) and northern (PCN) polar caps: Consistency and discrepancy. *Geophysical Research Letters*, *29*(18), 26–1–26–4. Retrieved 2022-12-18, from http://doi.wiley.com/10.1029/2002GL015179 doi: 10.1029/2002GL015179

Lyatsky, W., Newell, P. T., & Hamza, A. (2001). Solar illumination as cause of the equinoctial preference for geomagnetic activity. *Geophysical Research Letters*, *28*(12), 2353–2356. Retrieved 2022-11-27, from http://doi.wiley.com/10.1029/2000GL012803 doi: 10.1029/2000GL012803

Maezawa, K. (1976). Magnetospheric convection induced by the positive and negative *Z* components of the interplanetary magnetic field: Quantitative analysis using polar cap magnetic records. *Journal of Geophysical Research*, *81*(13), 2289–2303. Retrieved 2023-02-24, from http://doi.wiley.com/10.1029/JA081i013p02289 doi: 10.1029/JA081i013p02289

Matzka, J., & Troshichev, O. (2014). *The Polar Cap North (PCN) index.* DTU Space, Geomagnetism. Retrieved 2023-04-19, from https://www.space.dtu.dk/wdc/pcn-index doi: 10.11581/DTU:00000057

McCreadie, H., & Menvielle, M. (2010). The PC index: review of methods. *Annales Geophysicae*, *28*(10), 1887–1903. Retrieved 2022-12-18, from https://angeo.copernicus.org/articles/28/1887/2010/ doi:

10.5194/angeo-28-1887-2010
Meng, X.-L., Rosenthal, R., & Rubin, D. (1992). Comparing correlated correlation coefficients. *Psychological Bulletin*, *111*(1), 172–175. Retrieved 2023-02-21, from http://doi.apa.org/getdoi.cfm?doi=10.1037/0033-2909.111.1.172 doi: 10.1037/0033-2909.111.1.172
Menvielle, M., McCreadie, H., & Demetrescu, C. (2013). *Recommendation #3 - recommendation by the task force: Fully recommend endorsement of the pc index* (Tech. Rep.). IAGA 12th Scientific Assembly, Mérida, Yucatán, Mexico: International Association of Geomagnetism and Aeronomy, IAGA_documentation_20130225.pdf.
Merkine, V. G., Papadopoulos, K., Milikh, G., Sharma, A. S., Shao, X., Lyon, J., & Goodrich, C. (2003). Effects of the solar wind electric field and ionospheric conductance on the cross polar cap potential. *Geophysical Research Letters*, *30*(23), n/a–n/a. Retrieved 2022-12-09, from http://doi.wiley.com/10.1029/2003GL017903 doi: 10.1029/2003GL017903
Milan, S. E., Carter, J. A., Bower, G. E., Imber, S. M., Paxton, L. J., Anderson, B. J., . . . Hubert, B. (2020). Dual-lobe reconnection and horse-collar auroras. *Journal of Geophysical Research: Space Physics*, *125*(10). Retrieved 2023-01-24, from https://onlinelibrary.wiley.com/doi/10.1029/2020JA028567 doi: 10.1029/2020JA028567
Milan, S. E., Carter, J. A., Sangha, H., Bower, G. E., & Anderson, B. J. (2021). Magnetospheric flux throughput in the Dungey cycle: Identification of convection state during 2010. *Journal of Geophysical Research: Space Physics*, *126*(2), e2020JA028437. Retrieved from https://agupubs.onlinelibrary.wiley.com/doi/abs/10.1029/2020JA028437 doi: https://doi.org/10.1029/2020JA028437
Morley, S. K., & Lockwood, M. (2005). A numerical model of the ionospheric signatures of time-varying magnetic reconnection: 2. Measuring expansions in the ionospheric flow response. *Annales Geophysicae*, *23*(7), 2501–2510. Retrieved 2022-08-18, from https://angeo.copernicus.org/articles/23/2501/2005/ doi: 10.5194/angeo-23-2501-2005
Nagatsuma, T. (2002). Characteristics of negative values of polar cap index as an indicator of reversed convection. *Adv. Polar Upper Atmos. Res*, *16*, 36-44. Retrieved 2023-02-23, from http://polaris.nipr.ac.jp/~uap/apuar/apuar16/Nagatsuma16-03.pdf
Nagatsuma, T. (2004). Conductivity dependence of cross-polar potential saturation. *Journal of Geophysical Research*, *109*(A4), A04210. Retrieved 2023-02-23, from http://doi.wiley.com/10.1029/2003JA010286 doi: 10.1029/2003JA010286
Newell, P. T., Sotirelis, T., Skura, J., Meng, C.-I., & Lyatsky, W. (2002). Ultraviolet insolation drives seasonal and diurnal space weather variations. *Journal of Geophysical Research*, *107*(A10), 1305. Retrieved 2022-12-09, from http://doi.wiley.com/10.1029/2001JA000296 doi: 10.1029/2001JA000296
Orr, L., Grocott, A., Walach, M., Chisham, G., Freeman, M., Lam, M., & Shore, R. (2022). A quantitative comparison of high latitude electric field models during a large geomagnetic storm. *Space Weather*. Retrieved 2022-12-27, from https://onlinelibrary.wiley.com/doi/10.1029/2022SW003301 doi: 10.1029/2022SW003301
Pettigrew, E. D., Shepherd, S. G., & Ruohoniemi, J. M. (2010). Climatological patterns of high-latitude convection in the Northern and Southern hemispheres: Dipole tilt dependencies and interhemispheric comparisons. *Journal of Geophysical Research: Space Physics*, *115*(A7). Retrieved 2023-02-24, from http://doi.wiley.com/10.1029/2009JA014956 doi: 10.1029/2009JA014956
Raeder, J., Wang, Y., Fuller-Rowell, T., & Singer, H. (2001). Global simulation of

magnetospheric space weather effects of the Bastille day storm. *Solar Physics*, *204*(1/2), 323–337. Retrieved 2022-12-09, from http://link.springer.co/10.1023/A:1014228230714 doi: 10.1023/A:1014228230714

Reistad, J. P., Laundal, K. M., Østgaard, N., Ohma, A., Burrell, A. G., Hatch, S. M., ... Thomas, E. G. (2021). Quantifying the lobe reconnection rate during dominant IMF B_y periods and different dipole tilt orientations. *Journal of Geophysical Research: Space Physics*, *126*(11). Retrieved 2022-12-19, from https://onlinelibrary.wiley.com/doi/10.1029/2021JA029742 doi: 10.1029/2021JA029742

Reistad, J. P., Laundal, K. M., Østgaard, N., Ohma, A., Thomas, E. G., Haaland, S., ... Milan, S. E. (2019). Separation and quantification of ionospheric convection sources: 2. The dipole tilt angle influence on reverse convection cells during northward IMF. *Journal of Geophysical Research: Space Physics*, *124*(7), 6182–6194. Retrieved 2023-02-20, from https://onlinelibrary.wiley.com/doi/10.1029/2019JA026641 doi: 10.1029/2019JA026641

Rich, F., & Hairston, M. (1994). Large-scale convection patterns observed by DMSP. *Journal of Geophysical Research*, *99*(A3), 3827–3844. Retrieved 2023-02-24, from http://doi.wiley.com/10.1029/93JA03296 doi: 10.1029/93JA03296

Ridley, A. J., Gombosi, T. I., & DeZeeuw, D. L. (2004). Ionospheric control of the magnetosphere: conductance. *Annales Geophysicae*, *22*(2), 567–584. Retrieved 2022-11-10, from https://angeo.copernicus.org/articles/22/567/2004/ doi: 10.5194/angeo-22-567-2004

Ridley, A. J., & Kihn, E. A. (2004). Polar cap index comparisons with AMIE cross polar cap potential, electric field, and polar cap area. *Geophysical Research Letters*, *31*(7), n/a–n/a. Retrieved 2022-12-18, from http://doi.wiley.com/10.1029/2003GL019113 doi: 10.1029/2003GL019113

Ruohoniemi, J. M., & Greenwald, R. A. (2005). Dependencies of high-latitude plasma convection: Consideration of interplanetary magnetic field, seasonal, and universal time factors in statistical patterns. *Journal of Geophysical Research: Space Physics*, *110*(A9). Retrieved 2022-12-19, from http://doi.wiley.com/10.1029/2004JA010815 doi: 10.1029/2004JA010815

Russell, C. T., Luhmann, J. G., & Lu, G. (2001). Nonlinear response of the polar ionosphere to large values of the interplanetary electric field. *Journal of Geophysical Research: Space Physics*, *106*(A9), 18495–18504. Retrieved 2022-12-09, from http://doi.wiley.com/10.1029/2001JA900053 doi: 10.1029/2001JA900053

Russell, C. T., & McPherron, R. L. (1973). Semiannual variation of geomagnetic activity. *Journal of Geophysical Research*, *78*(1), 92–108. Retrieved 2022-11-03, from http://doi.wiley.com/10.1029/JA078i001p00092 doi: 10.1029/JA078i001p00092

Saunders, M. A., Freeman, M. P., Southwood, D. J., Cowley, S. W. H., Lockwood, M., Samson, J. C., ... Hughes, T. J. (1992). Dayside ionospheric convection changes in response to long-period interplanetary Magnetic field oscillations: Determination of the ionospheric phase velocity. *Journal of Geophysical Research*, *97*(A12), 19373. Retrieved 2022-08-18, from http://doi.wiley.com/10.1029/92JA01383 doi: 10.1029/92JA01383

Shepherd, S. G. (2007). Polar cap potential saturation: Observations, theory, and modeling. *Journal of Atmospheric and Solar-Terrestrial Physics*, *69*(3), 234–248. Retrieved 2022-12-09, from https://linkinghub.elsevier.com/retrieve/pii/S136468260600263X doi: 10.1016/j.jastp.2006.07.022

Shepherd, S. G. (2014). Altitude-adjusted corrected geomagnetic coordinates: Definition and functional approximations. *Journal of Geophysical Research: Space Physics*, *119*(9), 7501–7521. Retrieved 2023-02-15, from C doi: 10.1002/

2014JA020264

Siscoe, G. L. (2002). Hill model of transpolar potential saturation: Comparisons with MHD simulations. *Journal of Geophysical Research*, *107*(A6), 1075. Retrieved 2022-12-09, from http://doi.wiley.com/10.1029/2001JA000109 doi: 10.1029/2001JA000109

Siscoe, G. L., & Huang, T. S. (1985). Polar cap inflation and deflation. *Journal of Geophysical Research: Space Physics*, *90*(A1), 543–547. Retrieved 2023-02-20, from http://doi.wiley.com/10.1029/JA090iA01p00543 doi: 10.1029/JA090iA01p00543

Sivadas, N., & Sibeck, D. (2022). Regression bias in using solar wind measurements. *Frontiers in Astronomy and Space Sciences*, *9*, 924976. Retrieved 2022-07-07, from https://www.frontiersin.org/articles/10.3389/fspas.2022.924976/full doi: 10.3389/fspas.2022.924976

Sivadas, N., Sibeck, D., Subramanyan, V., Walach, M.-T., Murphy, K., & Halford, A. (2022). Uncertainty in solar wind forcing explains polar cap potential saturation. *arXiv*. Retrieved 2023-02-22, from https://arxiv.org/abs/2201.02137 doi: 10.48550/ARXIV.2201.02137

Southwood, D. J. (1987). The ionospheric signature of flux transfer events. *Journal of Geophysical Research*, *92*(A4), 3207. Retrieved 2022-11-11, from http://doi.wiley.com/10.1029/JA092iA04p03207 doi: 10.1029/JA092iA04p03207

Stauning, P. (2013). The Polar Cap index: A critical review of methods and a new approach. *Journal of Geophysical Research: Space Physics*, *118*(8), 5021–5038. Retrieved 2022-12-18, from https://onlinelibrary.wiley.com/doi/10.1002/jgra.50462 doi: 10.1002/jgra.50462

Stauning, P. (2018). Multi-station basis for Polar Cap (PC) indices: ensuring credibility and operational reliability. *Journal of Space Weather and Space Climate*, *8*, A07. Retrieved 2023-04-19, from https://www.swsc-journal.org/10.1051/swsc/2017036 doi: 10.1051/swsc/2017036

Stauning, P. (2021a). The Polar Cap (PC) index combination, PCC: relations to solar wind properties and global magnetic disturbances. *Journal of Space Weather and Space Climate*, *11*, 19. Retrieved 2023-02-18, from https://www.swsc-journal.org/10.1051/swsc/2020074 doi: 10.1051/swsc/2020074

Stauning, P. (2021b). Transpolar convection and magnetospheric ring current relations: Real-time applications of the polar cap (PC) indices. *Space Weather*, *19*(7). Retrieved 2022-12-19, from https://onlinelibrary.wiley.com/doi/10.1029/2020SW002702 doi: 10.1029/2020SW002702

Stauning, P. (2022a). Reply to comment by Troshichev et al. on “The use of invalid Polar Cap South (PCS) indices in publications”. *Journal of Geophysical Research: Space Physics*, *127*(10). Retrieved 2023-01-24, from https://onlinelibrary.wiley.com/doi/10.1029/2022JA030856 doi: 10.1029/2022JA030856

Stauning, P. (2022b). The use of invalid polar cap south (PCS) indices in publications. *Journal of Geophysical Research: Space Physics*, *127*(5). Retrieved 2023-02-18, from https://onlinelibrary.wiley.com/doi/10.1029/2022JA030355 doi: 10.1029/2022JA030355

Stauning, P., & Troshichev, O. (2008). Polar cap convection and PC index during sudden changes in solar wind dynamic pressure. *Journal of Geophysical Research: Space Physics*, *113*(A8), n/a–n/a. Retrieved 2022-11-11, from http://doi.wiley.com/10.1029/2007JA012783 doi: 10.1029/2007JA012783

Stubbs, T. J., Lockwood, M., Cargill, P., Fennell, J., Grande, M., Kellett, B., ... Rees, A. (2001). Dawn-dusk asymmetry in particles of solar wind origin within the magnetosphere. *Annales Geophysicae*, *19*(1), 1–9. Retrieved 2022-08-18, from https://angeo.copernicus.org/articles/19/1/2001/ doi: 10.5194/angeo-19-1-2001

Sundberg, K., Cumnock, J. A., & Blomberg, L. G. (2009). Reverse convection potential: A statistical study of the general properties of lobe reconnection and saturation effects during northward IMF. *Journal of Geophysical Research: Space Physics*, *114*(A6), A06205. Retrieved 2023-02-24, from `http://doi.wiley.com/10.1029/2008JA013838` doi: 10.1029/2008JA013838

Tanaka, T. (2007). Magnetosphere–ionosphere convection as a compound system. *Space Science Reviews*, *133*(1-4), 1–72. Retrieved 2022-11-10, from `https://link.springer.com/10.1007/s11214-007-9168-4` doi: 10.1007/s11214-007-9168-4

Thomas, E. G., & Shepherd, S. G. (2018). Statistical patterns of ionospheric convection derived from mid-latitude, high-latitude, and polar SuperDARN HF radar observations. *Journal of Geophysical Research: Space Physics*, *123*(4), 3196–3216. Retrieved 2023-02-24, from `https://onlinelibrary.wiley.com/doi/10.1002/2018JA025280` doi: 10.1002/2018JA025280

Troshichev, O. (2022). PC index as a ground-based indicator of the solar wind energy incoming into the magnetosphere: (1) relation of PC index to the solar wind electric field EKL. *Frontiers in Astronomy and Space Sciences*, *9*, 1069470. Retrieved 2023-02-19, from `https://www.frontiersin.org/articles/10.3389/fspas.2022.1069470/full` doi: 10.3389/fspas.2022.1069470

Troshichev, O., & Andrezen, V. (1985). The relationship between interplanetary quantities and magnetic activity in the southern polar cap. *Planetary and Space Science*, *33*(4), 415–419. Retrieved 2023-02-19, from `https://linkinghub.elsevier.com/retrieve/pii/0032063385900868` doi: 10.1016/0032-0633(85)90086-8

Troshichev, O., Andrezen, V., Vennerstrøm, S., & Friis-Christensen, E. (1988). Magnetic activity in the polar cap—A new index. *Planetary and Space Science*, *36*(11), 1095–1102. Retrieved 2022-12-18, from `https://linkinghub.elsevier.com/retrieve/pii/0032063388900633` doi: 10.1016/0032-0633(88)90063-3

Troshichev, O., Dolgacheva, S., & Sormakov, D. (2022b). Invariability of relationships between the solar wind electric field E and the magnetic activity indices PC, AL and Dst. *Journal of Atmospheric and Solar-Terrestrial Physics*, *235*, 105894. Retrieved 2023-02-19, from `https://linkinghub.elsevier.com/retrieve/pii/S1364682622000682` doi: 10.1016/j.jastp.2022.105894

Troshichev, O., Dolgacheva, S. A., & Sormakov, D. A. (2022a). Comment on "The use of invalid Polar Cap South (PCS) indices in publications" by Stauning. *Journal of Geophysical Research: Space Physics*, *127*(10). Retrieved 2023-01-24, from `https://onlinelibrary.wiley.com/doi/10.1029/2022JA030820` doi: 10.1029/2022JA030820

Troshichev, O., & Janzhura, A. (2012). Physical implications of discrepancy between summer and winter PC indices observed in the course of magnetospheric substorms. *Advances in Space Research*, *50*(1), 77–84. Retrieved 2023-02-20, from `https://linkinghub.elsevier.com/retrieve/pii/S0273117712001974` doi: 10.1016/j.asr.2012.03.017

Troshichev, O., Janzhura, A., & Stauning, P. (2006). Unified PCN and PCS indices: Method of calculation, physical sense, and dependence on the IMF azimuthal and northward components. *Journal of Geophysical Research*, *111*(A5), A05208. Retrieved 2022-12-18, from `http://doi.wiley.com/10.1029/2005JA011402` doi: 10.1029/2005JA011402

Troshichev, O., Janzhura, A., & Stauning, P. (2007). Reply to comment by R. Lukianova on "Unified PCN and PCS indices: Method of calculation, physical sense, dependence on the IMF azimuthal and northward components". *Journal of Geophysical Research: Space Physics*, *112*(A7), n/a–n/a. Retrieved 2023-02-20, from `http://doi.wiley.com/10.1029/2006JA012029` doi:

10.1029/2006JA012029

Vasyliunas, V., Kan, J., Siscoe, G., & Akasofu, S.-I. (1982). Scaling relations governing magnetospheric energy transfer. *Planetary and Space Science*, *30*(4), 359–365. Retrieved 2023-02-26, from https://linkinghub.elsevier.com/retrieve/pii/0032063382900411 doi: 10.1016/0032-0633(82)90041-1

Vennerstrøm, S. (2019). *The geomagnetic activity index pc* (Doctoral dissertation, Geophysical Institute, University of Copenhagen; Danish Meteorological Institute DMI Scientific Report 91-3). Retrieved 2022-11-03, from https://www.dmi.dk/fileadmin/user_upload/Rapporter/SR/1991/sr91-3.pdf

Wang, H., & Lühr, H. (2007). Seasonal-longitudinal variation of substorm occurrence frequency: Evidence for ionospheric control. *Geophysical Research Letters*, *34*(7), L07104. Retrieved 2022-11-27, from http://doi.wiley.com/10.1029/2007GL029423 doi: 10.1029/2007GL029423

Weimer, D. R. (2001). Maps of ionospheric field-aligned currents as a function of the interplanetary magnetic field derived from Dynamics Explorer 2 data. *Journal of Geophysical Research: Space Physics*, *106*(A7), 12889–12902. Retrieved 2023-02-24, from http://doi.wiley.com/10.1029/2000JA000295 doi: 10.1029/2000JA000295

Wilder, F. D., Clauer, C. R., & Baker, J. B. H. (2009). Reverse convection potential saturation during northward IMF under various driving conditions. *Journal of Geophysical Research: Space Physics*, *114*(A8), A08209. Retrieved 2023-02-24, from http://doi.wiley.com/10.1029/2009JA014266 doi: 10.1029/2009JA014266

Wilder, F. D., Clauer, C. R., & Baker, J. B. H. (2010). Polar cap electric field saturation during interplanetary magnetic field B $_Z$ north and south conditions. *Journal of Geophysical Research: Space Physics*, *115*(A10), A10230. Retrieved 2023-02-24, from http://doi.wiley.com/10.1029/2010JA015487 doi: 10.1029/2010JA015487

Zhang, B., Lotko, W., Brambles, O., Wiltberger, M., & Lyon, J. (2015). Electron precipitation models in global magnetosphere simulations. *Journal of Geophysical Research: Space Physics*, *120*(2), 1035–1056. Retrieved 2022-12-09, from https://onlinelibrary.wiley.com/doi/10.1002/2014JA020615 doi: 10.1002/2014JA020615

Zhang, Q.-H., Zhang, Y.-L., Wang, C., Oksavik, K., Lyons, L. R., Lockwood, M., … Xia, L.-D. (2021). A space hurricane over the Earth's polar ionosphere. *Nature Communications*, *12*(1), 1207. Retrieved 2022-08-18, from http://www.nature.com/articles/s41467-021-21459-y doi: 10.1038/s41467-021-21459-y

Zhao, H., & Zong, Q.-G. (2012). Seasonal and diurnal variation of geomagnetic activity: Russell-McPherron effect during different IMF polarity and/or extreme solar wind conditions. *Journal of Geophysical Research: Space Physics*, *117*(A11), n/a–n/a. Retrieved 2022-12-29, from http://doi.wiley.com/10.1029/2012JA017845 doi: 10.1029/2012JA017845

8 Open Research

The data used in this study are all openly available. The interplanetary data are available from the Physics Data Facility (SPDF) at NASA's Goddard Space Flight Center as the Omni composite from https://omniweb.gsfc.nasa.gov/ow_min.html. The polar cap indices are available from the International Service of Geomagnetic Indices (ISGI) at http://isgi.unistra.fr/data_download.php.

Acknowledgments

The author is grateful to the instrument scientists and engineers who make the datasets employed in this study possible; in particular those at the National Space Institute, Technical University of Denmark (DTU, Denmark) for the *PCN* index and the Arctic and Antarctic Research Institute (AARI, Russian Federation) for the *PCS* index. He is also grateful to the SuperDARN project. SuperDARN is a collection of radars funded by national scientific funding agencies of Australia, Canada, China, France, Italy, Japan, Norway, South Africa, United Kingdom and the United States of America: he particularly thanks Kathryn McWilliams of University of Saskatchewan for the generation of the SuperDARN transpolar voltage dataset used. He also thanks the staff of the datacentres that allow easy access to the data. These include: the Space Physics Data Facility (SPDF) at NASA's Goddard Space Flight Center for the Omni composite of interplanetary observations; the International Service of Geomagnetic Indices (ISGI), France and collaborating institutes for distribution of the polar cap indices. This work is supported by a number of grants: consolidated grants number ST/R000921/1 and ST/V000497/1 from the United Kingdom Science and Technology Facilities Council (UKRI/STFC) and the SWIGS Directed Highlight Topic Grant number NE/P016928/1/ and grant NE/S010033/1 from the United Kingdom Natural Environment Research Council (UKRI/NERC).